



1 Holocene vegetation dynamics in response to climate change and hydrological processes  
2 in the Bohai region

3 Chen Jinxia<sup>a,b,\*</sup>, Shi Xuefa<sup>a,b,\*</sup>, Liu Yanguang<sup>a,b</sup>, Qiao Shuqing<sup>a,b</sup>, Yang Shixiong<sup>c,d</sup>, Yan Shijuan<sup>a,b</sup>, Lv Huahua<sup>a,b</sup>, Li  
4 Xiaoyan<sup>a,b</sup>, Li Chaoxin<sup>a,b</sup>

5 <sup>a</sup> Key Laboratory of Marine Sedimentology and Environmental Geology, First Institute of Oceanography, SOA, Qingdao 266061, China

6 <sup>b</sup> Laboratory for Marine Geology, Qingdao National Laboratory for Marine Science and Technology, Qingdao 266061, China

7 <sup>c</sup> Key Laboratory of Coastal Wetland Biogeosciences, China Geologic Survey, Qingdao 266071, Shandong, China

8 <sup>d</sup> Laboratory for Marine Geology, Qingdao National Laboratory for Marine Science and Technology, Qingdao, 266061, China

9

10 \* Corresponding author at: Key Laboratory of Marine Sedimentology and Environmental Geology, First Institute of Oceanography, SOA, Qingdao 266061, China.

11 E-mail address: jinxiachen@fio.org.cn (J. Chen); xfshi@fio.org.cn (X. Shi).

12 **ABSTRACT**

13 Coastal vegetation not only mitigates the damage inflicted by marine disasters on coastal area, but also plays an  
14 important role in the global carbon cycle (i.e. blue carbon). Nevertheless, detailed records of both long-term changes in  
15 coastal vegetation composition and diversity, coupled with climate change and river evolution, remain sparse. To  
16 explore vegetation dynamics and their influencing factors on the coastal area of the Bohai Sea (BS) during the  
17 Holocene, in this study, we present high-resolution pollen and grain size data obtained from a sediment core of the BS.  
18 The results reveal that two rapid and abrupt changes in salt marsh vegetation are linked with the river-system changes.  
19 Within each event, a recurring pattern—starting with a decline in *Cyperaceae*, followed by an increase in *Artemisia*  
20 and *Chenopodiaceae*—suggests a successional process that is determined by the close relationship between Yellow  
21 River (YR) channel shifts and the wetland community dynamics. The phreatophyte *Cyperaceae* at the base of each  
22 sequence indicate lower saline conditions. Unchannelized river flow characterized the onset of the YR channel shift,  
23 caused a huge river-derived sediment accumulation in the floodplain, and destroyed the sedges in the coastal  
24 depression. Along with the formation of a new channel, lateral migration of the lower channel stopped, and a new  
25 intertidal mudflat was formed. Pioneer species (*Chenopodiaceae*, *Artemisia*) were the first to colonize the bare zones of



26 the lower and middle marsh areas. In addition, the pollen results revealed that the vegetation in the Shandong  
27 Peninsula was dominated by broadleaved trees during the early Holocene (8500–6500 a BP) and by conifers and  
28 broadleaved forests in the middle Holocene (6500–3500 a BP), which was followed by an expansion of broadleaved  
29 trees (3500–1000 a BP). After 1000 a BP, human impacts are recognized as a sudden decrease in *Quercus* and a  
30 marked increase in secondary vegetation *Pinus*. The pollen-based temperature index indicated that a warmer early and  
31 late Holocene and colder middle Holocene were consistent with previously reported temperature records for North and  
32 Northwest China. The main driving factors of temperature variation in this region are insolation, greenhouse gases and  
33 the El Niño-Southern Oscillation.

34

35 *Keywords:* Coastal salt marsh; Pollen; Delta superlobe; Temperature; El Niño-Southern Oscillation

36

## 37 1. Introduction

38 Coastal areas are important habitats for civilizations, and they are playing an increasingly critical role in trade  
39 globalization (Hemavathi et al., 2019). Because they are located between marine ecosystems and terrestrial ecosystems,  
40 coastal area are prone to many natural hazards such as flooding, storms and tsunamis (Hou and Hou, 2020). Coastal  
41 vegetation, which acts as a natural barrier, is widely distributed in coastal areas and could effectively mitigate the  
42 damage of marine disasters to the economy and environment of coastal areas (Zhang et al., 2018). Moreover, despite  
43 their relatively small global extent (between 0.5 and  $1 \times 10^6$  km<sup>2</sup>), coastal vegetation ecosystems, tidal marshes,  
44 mangroves, and seagrasses play an important role in the global carbon cycle (Serrano et al., 2019; Spivak et al., 2019).  
45 Their organic carbon sequestration rates exceed those of terrestrial forests, per unit area, by 1–2 orders of magnitude,  
46 and contribute ~50% of C sequestered in marine sediments (Serrano et al., 2019). Hence, it is important to understand  
47 the long-term spatial–temporal dynamics of coastal vegetation, which are favorable for the global carbon cycle  
48 research and coastal restoration.

49 Climatic fluctuation, post glacial sea-level rise and changes in river discharge provoked dramatic habitat changes  
50 along coastal areas during the Late Pleistocene and Holocene (Neumann et al., 2010; Cohen et al., 2012; Pessenda et



51 al., 2012; França et al., 2015). Presently, the relationship of sea-level change and coastal vegetation (especially  
52 mangrove) evolution has been studied by many researchers (e.g. Engelhart et al., 2007; Gonzalez and Dupont, 2009;  
53 França et al., 2012; Woodroffe et al., 2015; Hendy et al., 2016). However, studies on the long-term dynamics of coastal  
54 vegetation, coupled with climate change and river evolution, are sparse. The global rivers delivered large amounts of  
55 material to the ocean in the Holocene; the total suspended sediment delivered by all rivers to the ocean was  
56 approximately  $13.5 \times 10^9$  tons annually (Milliman and Meade, 1983). The material transported by the rivers had huge  
57 impacts on the coastal ecosystem. Hence, a deeper understanding of correlations between coastal vegetation and river  
58 variables is required to better assess coastal vegetation responses to global warming in the future.

59 In the coastal areas of the BS, vegetation is dominated by warm temperate deciduous broadleaved forests and  
60 shrub grasslands (Wang et al., 1993). The YR, as the second largest river in the world in terms of sediment discharge  
61 (Milliman and Meade, 1983), transports large amounts of sediment into the BS every year; hence, it has developed a  
62 delta complex in the west coastal region of the BS since 7 ka BP (He et al., 2019). Deposition of the Yellow River delta  
63 (YRD) complex resulted in the form of a vast area of floodplain and estuarine wetland (Xue et al., 1995; Cui et al.,  
64 2009; Liu et al., 2009). Based on the study of coastal vegetation of the BS, it is helpful to understand the spatial and  
65 temporal drivers of ecological variability, and thus of the vegetation-climate and river relationship, especially wetland  
66 dynamics. However, few related investigations, which can potentially provide a better understanding of the vegetation  
67 dynamics and their response to climate and river variables, have been conducted in the Bohai region.

68 Pollen records have been useful in terms of reconstructing vegetation dynamics and environmental changes  
69 associated with climatic changes in the geological record (Bao et al., 2007; Cohen et al., 2008; Giraldo-Giraldo et al.,  
70 2018). Therefore, in this study, we carried out a detailed investigation of core sediments from Laizhou Bay, BS. We  
71 analyzed pollen and grain size proxies under high resolution and refined the chronology of the core by  $^{137}\text{Cs}$  and  
72  $\text{AMS }^{14}\text{C}$  dates. With this in mind, the specific objectives of the current research are formulated as follows: (1) to  
73 reconstruct the vegetation evolution history in the Bohai region and (2) to discuss tentatively the effects of climate and  
74 environment on coastal vegetation (especially wetlands) during the Holocene.

75



## 76 2. Study area

### 77 2.1. Geographical settings

78 The BS, a shallow inland sea in China, is connected with the Yellow Sea through the narrow Bohai Strait (Figure  
79 1). The main rivers flowing into the BS are the YR, Haihe River, Luanhe River, and Liaohe River. Among these, the  
80 YR is the largest and is the main source of sediments in this region. Over the past 2000 years, the YR has annually  
81 provided approximately  $1.1 \times 10^9$  tons of sediment discharged into the BS (Milliman et al., 1987). This immense  
82 amount of sediment has resulted in the rapid seaward progradation of YRD, and a rapid change in the location of the  
83 main distributaries in the lower delta plain.

84 The tidal current plays a critical role in the transportation and distribution of sediments in the BS. The tidal  
85 currents of the modern BS are dominated by semi-diurnal tides. The velocity of tidal currents varies from 20 to 80 cm/s.  
86 Three strong tidal current areas are observed in the northern Bohai Strait, central part of Bohai Bay, and eastern part of  
87 Liaodong Bay (Huang et al., 1999). In Laizhou Bay close to the core location, the speed of tidal currents is weak (Gu  
88 and Xiu, 1996).

89 The wind waves off the YRD are dominated by the East Asian monsoon and show significant seasonal variations.  
90 The prevailing northerly winds are much stronger in winter than the dominant southerly winds in summer. Strong  
91 winter winds induce strong wind waves, and thus cause strong bottom shear stresses which readily erode seabed  
92 sediment into water (Yang et al., 2011; Wang et al., 2014; Zhou et al., 2017).

93 The circulation of the BS is weak and the mean flow velocity is small. In winter, the predominant extension of the  
94 Yellow Sea Warm Current (YSWC) intrudes and crosses the Bohai Strait, moving westward along the central part of  
95 the BS and splits into two branches. One branch moves toward the northeast to form a clockwise gyre, and the other  
96 veers southward and then turns eastward along the southern coast to form a counterclockwise gyre. In summer, the  
97 YSWC disappears in the BS. Eddies generated in the BS are stronger than in winter. During this time, the central eddy  
98 is missing, the eddy in Laizhou Bay is more pronounced, and the coastal current along the southern and western  
99 coastlines of the BS is established (Figure 1b; Liu et al., 2015; Yang et al., 2016).



## 101 2.2. Climate and vegetation

102 The Bohai region lies in a zone of warm temperate monsoonal climate with distinctive seasons. The annual mean  
103 air temperature is 7.5–14.0 °C, and the annual average precipitation is 500–900 mm. As the Liaodong peninsula and  
104 Shandong peninsula protrude into the sea, they are clearly influenced by its proximity and experience sufficient rainfall.  
105 However, there is less rainfall in the mountain area of the northern part (Wang et al., 1993).

106 The regional vegetation is dominated by warm temperature deciduous broadleaved forests and shrub grasslands.  
107 Currently, natural vegetation only remains in the mountain areas because of widespread anthropogenic activities (e.g.  
108 cultivation and farming). The predominant deciduous broadleaved species belong to *Quercus*, such as *Q. liaotungensis*,  
109 *Q. dentata*, *Q. acutissima*, and *Q. variabilis*. Co-dominant plants are *Pinus*, including *P. densiflora* that grows in the  
110 coastal humid area, and *P. tabulaeformis* that is distributed in the relatively dry North China plain. In the plain area,  
111 apart from *P. tabulaeformis*, there are some deciduous broadleaved trees, such as *Ailanthus altissima*, *Koelreuteria*  
112 *paniculata*, and *Morus alba*. Other broadleaved trees, *Betula ermanii*, *Populus tremula*, *Acer* spp., *Tilia amurensis*, and  
113 *Carpinus turczaninowii* are distributed in the hills and lowlands (Wang et al., 1993). The coastal wetlands are occupied  
114 by herbs and shrubs, such as *Tamarix chinensis*, *Salix matsudana*, *S. integra*, *Phragmites australis*, *Aeluropus Trin*,  
115 *Limonium sinense*, *Suaeda glauca*, *Typha orientalis*, and *Acorus calamus* (Li et al., 2007; Xu et al., 2010).

116

## 117 3. Materials and methods

### 118 3.1. Core ection, sub-sampling, and chronology

119 Core CJ06-435 was collected in Laizhou Bay, BS in August 2007 by the R/V *Kan407* of the Shanghai Bureau.  
120 The core site is located at 37.50°N, 119.52°E, at a water depth of 14.6 m (Figure 1), with a length of 271 cm. In the  
121 laboratory, the core was spilt into two sections, photographed, macroscopically described, and sub-sampled.

122 Isotopes  $^{137}\text{Cs}$  and  $^{210}\text{Pb}$  were measured employing EG&G Ortec Gamma Spectrometry at the Nanjing Institute  
123 of Limnology and Geography, Chinese Academy of Sciences (NIGLAS).  The sediment samples were air-dried and  
124 pulverized.  $^{137}\text{Cs}$  and  $^{210}\text{Pb}$  concentrations were then determined from gamma emissions at 662 and 46.5 keV,  
125 respectively. In addition, a total of 10 samples consisting of foraminifera were obtained from the core for radiocarbon 



126 dating. The radiocarbon dating was conducted at the Woods Hole Oceanographic Institution (WHOI) and Beta  
127 Analytic Inc., USA. Radiocarbon dates were corrected for the regional marine reservoir effect ( $\Delta R = -139 \pm 59$  years,  
128 a regional average value determined for the BS) and calibrated using the Calib 7.04 program (Stuiver et al., 2019) with  
129 one standard deviation uncertainty ( $1.0 \times \sigma$ ) (Table 1).

130

### 131 3.2. Palynological and grain size sample analysis

132 A total of 127 samples were selected for pollen analyses. Approximately 3–5 g of b<sup>u</sup> sediments were taken  
133 from each sample, and a standard tablet of Lycopodium spores was added to each sample to calculate the pollen  
134 concentrations. Solutions of 15% HCl and 5% KOH were used to eliminate carbonates and to remove organic matter,  
135 respectively. Silicates were removed using 40% HF, and the residue was mounted in glycerin jelly. Fossil pollen was  
136 identified and counted with a light microscope at 400 $\times$  magnification. The percentage of each pollen type was  
137 calculated from the total palynomorph sum. The concentration values were calculated using the exotic pollen method,  
138 which is the number of pollen grains accumulated in 1.0 g of sediment.

139 Grain size analysis was performed at 2.0 cm intervals throughout the core using a Malvern Mastersizer 2000  
140 instrument at the laboratory of the First Institute of Oceanography. The chemical procedure of grain size experimental  
141 pretreatment was consistent with the procedures described by Chen et al. (2019a). A solution of 30% H<sub>2</sub>O<sub>2</sub> and 1.0  
142 mol/l were added to decompose the organic matter and remove carbonates.

143

## 144 4. Results

### 145 4.1. Chronological model

146 Measurements of <sup>137</sup>Cs and <sup>210</sup>Pb revealed activity at the top of the profile, indicating the recovery of recently  
147 deposited sediments. <sup>137</sup>Cs is a bomb-derived radionuclide, first appearing in environmental samples at measurable  
148 levels around 1954 with the onset of weapon testing (Kirchner and Ehlers, 1998), and was most prevalent in 1963 (the  
149 year of maximum fallout from atmospheric weapon testing) (Palinkas and Nittrouer, 2007). Subsurface peaks are not  
150 discernible in <sup>137</sup>Cs profiles of our study core (Figure 2). However, the deepest onset of <sup>137</sup>Cs is an effective marker of



151 the year 1954 (25 cm).

152 Often, the combined data of  $^{137}\text{Cs}$  and  $^{210}\text{Pb}_{\text{ex}}$  were used to calculate the sedimentation rates (Wu et al., 2015).  
153  $^{210}\text{Pb}_{\text{ex}}$  shows a downward decline owing to the decay of  $^{210}\text{Pb}$  when the sediment stably accumulates for an  
154 appropriate period, and the  $^{210}\text{Pb}_{\text{ex}}$  activity could be used to calculate the sedimentation rate. However, the  $^{210}\text{Pb}_{\text{ex}}$   
155 profiles of core CJ06-435 did not show a clear downward decline trend (Figure 2), and  $^{210}\text{Pb}_{\text{ex}}$  in the upper parts of the  
156 core is not that large when compared with the lower background values. Therefore, the  $^{210}\text{Pb}$  data seemed to be  
157 unsuitable for estimating the sedimentation rate of core CJ06-435. The  $^{137}\text{Cs}$ -derived average sedimentation rate was  
158 0.47 cm/yr in the upper 25 cm of core CJ06-435.

159 The results of AMS radiocarbon dating are shown in Table 1 and Figure 2. Three samples above the 20 cm depth  
160 were not included in the age model because their  $^{14}\text{C}$  age was anomalously greater than the  $^{137}\text{Cs}$  dating. The calibrated  
161 dates of several other samples are plotted against sediment depth and shown in Figure 3.

162

## 163 4.2. Palynology and grain size data

164 A total of 71 pollen taxa were identified in 127 samples of core CJ06-435. Pollen spectra are dominated by  
165 arboreal pollen (AP) in the middle and lower part (271–30 cm) of the core, primarily *Pinus* and *Quercus*. Other  
166 common arboreal genera are *Betula*, *Pterocarya*, Ulmaceae, and Moraceae. Nonarboreal pollen (NAP) is dominant in  
167 the upper part (30–0 cm) of the core. Among the NAP, Poaceae, Compositae, *Artemisia*, Chenopodiaceae, and  
168 Cyperaceae are most common. Fern spores are dominated by *Selaginella sinensis* and Polypodiaceae; however, their  
169 content is low throughout the core. CONISS analyses suggest that the pollen diagram can be divided into three zones  
170 (Figure 3 and 4).

171

### 172 4.2.1. Palynological zone 1 (271–156 cm)

173 This zone is characterized by a high content of broad-leaved trees, mostly consisting of *Quercus* (mean 18.7%),  
174 *Betula*, *Alnus*, *Pterocarya*, Ulmaceae and Moraceae. The content of conifer pollens is relatively low compared with  
175 other zones: *Pinus* ranges from 19.7% to 45.6% (mean 33.6%), and Taxodiaceae is present only occasionally. NAP of



176 Compositae (mean 1.2%), *Artemisia* (mean 4.2%), and Chenopodiaceae (mean 5.6%) have their lowest percentage in  
177 this zone, whereas Cyperaceae (mean 10.3%) and *Typha* (mean 11.2%) show the highest abundance (Figure 3). The  
178 palynological concentrations are high, varying between 6050 and 237 grains g<sup>-1</sup> (Figure 4).

179 The sediment of this zone is dominated by yellow-brown silt and clay silt with occasional sandy silt layers and  
180 shell fragments. The median grain size ranges between 5.3 φ and 7.1 φ, and the average value is approximately 5.9 φ  
181 (Figure 2).

182

#### 183 4.2.2. Palynological zone 2 (156–30 cm)

184 This zone can be further divided into four subzones according to the changing components of the pollen types.  
185 In 156 to 128 cm (subzone 2a), *Pinus* increases up to the highest abundance (mean 46.6%), whereas the content of  
186 broadleaved trees *Quercus* (16.1–9.5%, mean 14%), *Betula*, *Alnus*, *Pterocarya*, Ulmaceae, and Moraceae declines to  
187 different degrees. NAPs of Compositae (mean 2.5%), *Artemisia* (mean 6.6%), and Chenopodiaceae (mean 7.4%) have  
188 higher contents, whereas the percentages of Cyperaceae (mean 7.2%) and *Typha* (mean 3.1%) clearly decrease (Figure  
189 3). Total pollen concentration decreases notably in this subzone, especially during the interval of 156–135 cm when the  
190 value of total pollen concentrations (62–1306 grains/g, mean 485 grains/g) is the lowest in the entire core (Figure 4).

191 From 128 to 63 cm (subzone 2b), *Pinus* is present in lower amounts of approximately 49.4–27.3%. The *Betula*  
192 content slightly increases; however, the *Quercus* content decreases (18.1–7.9%, mean 13.5%). Small amounts of  
193 *Pterocarya*, Ulmaceae, and Moraceae appear occasionally. NAPs of Compositae, *Artemisia*, and Chenopodiaceae  
194 continuously increase in this interval to averages of 3.5%, 6.7%, and 12%, respectively. Poaceae, Cyperaceae, and  
195 *Typha* were present in largely unchanged proportions compared with subzone 2a (Figure 3). Pollen concentration  
196 increases up to a high abundance (mean 1260 grains/g) in this subzone (Figure 4).

197 From 63 to 41 cm (subzone 2c), the percentage frequency of *Pinus* is reduced upward, whereas that of *Quercus*  
198 (17.4–11.8%, mean 14.8%), *Betula*, *Alnus*, *Pterocarya*, and Ulmaceae increases. Similar to subzone 2b, this subzone  
199 has relatively high quantities of herb pollen such as Compositae, *Artemisia*, and Chenopodiaceae (Figure 3). Pollen  
200 concentrations were found to vary between 456 and 1381 grains/g (Figure 4).



201 In contrast, pollen subzone 2d (41–30 cm) is marked by a sudden decrease in the broadleaved tree pollen of  
202 *Quercus* (9.8%), and a steep increase of the conifer pollen of *Pinus* (41.1%), even though the percentage frequencies of  
203 the herbs are the same as those of subzone 2c (Figure 3). 

204 On the basis of the downcore distribution of grain size (Figure 2), zone 2 can be subdivided into three sections.  
205 Section 1 (156–135 cm) is characterized by yellow-brown sandy silt mixed with shell fragments. The median grain  
206 size ranges between 4.3  $\phi$  and 4.8  $\phi$ . Section 2 (135–83 cm) is composed mainly of yellow-brown silt with occasional  
207 sandy silt layers. Median grain size varies between 5.7  $\phi$  and 7.1  $\phi$ . Section 3 (83–30 cm) consists of yellow-brown  
208 clay silt and sandy silt, with shell fragments at 68–71 cm. The median grain size ranges between 5.3  $\phi$  and 6.4  $\phi$ .

209

#### 210 4.2.3. Palynological zone 3 (30–0 cm)

211 This zone is characterized by a notable decrease in AP and a rapid increase in NAP. The percentage of *Pinus* and  
212 *Quercus* pollens is the lowest in the core, averaging approximately 19.7% and 5.5%, respectively. The content of  
213 Poaceae, Compositae, *Artemisia*, and Chenopodiaceae increases in this zone, with average values of *Artemisia* and  
214 Chenopodiaceae reaching up to 24.6% and 21.1%, respectively (Figure 3). The total pollen concentration declines to  
215 188 grains/g in the lower part of the zone (30–19 cm) and then increases slightly (to approximately 621 grains/g) at the  
216 top (Figure 4). 

217 Based on the change of grain size, zone 3 can be subdivided into two sections. The upper section (30–19 cm) is  
218 characterized by soil-yellow sandy silt with many shell fragments occurring at 30–29 cm. The median grain size of the  
219 section ranges between 4.3  $\phi$  and 5.2  $\phi$ . The lower section (19–0 cm, median grain size 5.5  $\phi$ –6.8  $\phi$ ) consists of  
220 soil-yellow clay silt with sandy silt layers at some depths (Figure 2).

221

## 222 5. Discussion

### 223 5.1. Key terrestrial palynomorphic proxies of environmental and climatic change

224 In  our sediment core CJ06–435, both *Pinus* and *Quercus* pollen are predominant pollen types among the AP. This  
225 result is consistent with the pollen records in the surface sediments of Laizhou Bay (Yang et al., 2016). In surface



226 sediments from Laizhou Bay, higher concentrations of *Pinus* and *Quercus* pollen occur east of Laizhou Bay, and lower  
227 concentrations occur in the nearshore area outside the mouth of the YR (Figure 5a and b). This can be explained by the  
228 nearshore epicontinental vegetation of Laizhou Bay. In the low mountains and hilly area of Shandong Peninsula, the  
229 vegetation is represented chiefly by *Pinus densiflora* and *Quercus* spp. forests (Wang et al., 1993). The surface  
230 sediment concentration of *Pinus* and *Quercus* pollen grains is clearly increased near the Shandong Peninsula and is a  
231 good indicator of their parental plants on the peninsula. Modern research found that incremental temperature had  
232 negative impacts on radial growth of *P. densiflora* and positive impacts on that of *Quercus* spp. (Byun et al., 2013). For  
233 example, with the rise of annual mean temperature, *P. densiflora* forests have naturally decreased by approximately 4%  
234 in South Korea from 1996 to 2010, while *Quercus* spp. increased by 1.13% (Korea Forest Service, 2011; Kim et al.,  
235 2011). Therefore, the variations of *Pinus* and *Quercus* pollen in our sediment core from Laizhou Bay may be related to  
236 temperature change.

237 It is worth noting that *Pinus* pollen is a bisaccate grain. It has relatively high aerodynamic and hydrodynamic  
238 characteristics and can be transported efficiently by wind and water (Sander, 2001; Montade et al., 2011). Previous  
239 studies revealed that *Pinus* is represented in a small percentage nearshore and in a large percentage in the deep ocean  
240 (Zheng et al., 2011; Dai et al., 2014; Dai and Weng, 2015; Luo et al., 2014). Pollen distribution in the surface  
241 sediments of Laizhou Bay also shows that *Pinus* pollen decreases seaward along the inflowing rivers; however it  
242 increases in a northeasterly direction away from the coast (Yang et al., 2016). Hence, concerning *Pinus* pollen data,  
243 caution is required because climate variation alone may not be responsible for the change of *Pinus* pollen in marine  
244 sediment. Aerodynamic and hydrodynamic conditions may also influence the value of *Pinus* in sediments.

245 Herb pollen, especially Chenopodiaceae, also occupies an important position in core CJ06–435 (Figure 3). The  
246 spatial distribution of herb pollen suggests that higher concentrations occur in the nearshore area close to the YR  
247 estuary and the southwestern part of Laizhou Bay, and low concentrations are found in the east of Laizhou Bay (Figure  
248 5c and d). The YR is the main sediment source of the BS. The annual mean sediment load of the YR was  $1.08 \times 10^9$   
249 tons before dam construction (Milliman and Meade, 1983), 70–90% of which was deposited and formed a huge delta  
250 complex (Zhou et al., 2016). Natural vegetation in the modern YRD includes plenty of wetland herbs  chenopodiaceae



251 and *Artemisia* (Jiang et al., 2013). Furthermore, under the combined action of the ocean and rivers, alluvial plains and  
252 coast plains developed widely along the southern coast of Laizhou Bay. The terrestrial vegetation types in these areas  
253 change from a bare intertidal zone to seep weed swamp to reed swamp to cultivated land from the shoreline landward  
254 (Xu et al., 2010). Since the transportation distance for herb pollen is normally very short, its pollen concentration in  
255 samples close to the mouth of the YR and southwestern part of Laizhou Bay is much higher than in other samples  
256 (Figure 5 c and d), indicating that herb pollen of Laizhou Bay is mainly derived from the plant communities of the  
257 coastal wetlands. Therefore, we speculated that the herb pollen data in our sediment core might contain some  
258 information about the evolution of wetlands.

## 259

## 260 **5.2. Sedimentary records indicative of river channel shifts**

261 The most important geological events in the northern China coast after 7000 a BP were the shift of Yellow River  
262 channel and the formation of YRD. The YR has been easily plugged and breached, and therefore its lower reaches  
263 migrated because of its huge sediment load. The shifting of the lower reaches of the YR led to the formation of a new  
264 delta superlobe (He et al., 2019). Based on a study of cheniers and historical documents, nine YRD superlobes have  
265 been proposed by Xue and Cheng (1989) and Xue (1993) on the western shore of the BS. Among these, superlobe 1  
266 (7000–5000 a BP, He et al., 2019), superlobe 7 (11 AD–1048 AD, Xue, 1993), and superlobe 10 (1855 AD–present)  
267 are positioned near the core area in this study. The information about these superlobes formation are recorded in our  
268 core.

269 As shown in Figure 3 and 6e, herb percentage abruptly increased at 34 cm and 160 cm. Herb pollen in the  
270 sediment of Laizhou Bay is mainly derived from the coastal wetlands of the western BS. In 6000-7000 a BP and 1855  
271 AD, the YR emptied into the BS after a natural course shift, forming two huge delta at the western part of the BS  
272 (Saito et al., 2000). Wetland plants are the important vegetation type in the YRD (Jiang et al., 2013). The development  
273 of YRD wetland would change the amounts of herb pollen that was transported to the studied site. In addition, the  
274 formation of YRD caused the coastline to move closer to the position of the CJ06–435 core. Since most herb plants are  
275 small in size, their pollen grains are unable to disperse broadly (Chen et al., 2019b). The migration of the coastline



276 would change the availability of herb pollen to the studied site, and hence lead to variations of the pollen diagram.  
277 Therefore, we concluded that the abrupt change of herb pollen at 160 cm and 34 cm in core CJ06–435 is related to the  
278 formation of the YRD superlobe 1 and superlobe 10.

279 Compared with the pollen percentage, the pollen concentration can be interpreted in different ways. Namely, the  
280 percentage of different types of pollen is relative, whereas the pollen concentration is absolute, and it can directly  
281 reflect the amounts of pollen that were transported to the study area (Luo et al., 2013). Therefore, it is crucial that a  
282 correct interpretation of pollen data is based on a percentage diagram as well as concentration. In core CJ06–435, the  
283 concentrations of herbs—especially Chenopodiaceae and *Artemisia* (Figure 6f)—are higher at depths of 160–94 cm  
284 (6570–5000 a BP) and 34–0 cm (after 1855 AD), except for the two sections of 160–135 cm and 34–19 cm. A previous  
285 study noted that pollen grains would settle out of suspension in the same manner as suspended particles of fine silt and  
286 clay (Gail et al., 1999). The grain size data of core CJ06–435 revealed that coarser sediment occurred in the sections of  
287 160–135 cm and 34–19 cm (Figure 6a–d). Therefore, the extremely low pollen concentration in the sections of 160–  
288 135 cm and 34–19 cm is closely linked with the coarser sediment. Combined with the results of pollen percentage and  
289 grain size, we presumed that the higher herb pollen concentration in the periods of 6570–5000 a BP (160–94 cm) and  
290 after 1855 AD (34–0 cm) reflects changes in hydrographic conditions. Pollen data of surface sediments revealed that  
291 higher herb pollen concentrations occur in the YR, and the value of these concentrations show a decreasing trend  
292 starting from the river mouth towards the ocean. The distribution pattern of surface pollen revealed that the YR is a  
293 major carrier for most herbs taxa in the sediment of Laizhou Bay (Yang et al., 2016). At the site of core CJ06–435,  
294 which is close to the mouth of the YR in Laizhou Bay, higher herb pollen concentrations in the Holocene samples may  
295 indicate increased fluvial discharge.

296 Sediment grain size provides direct information on changes of the sediment source and the sedimentary  
297 environment (Friedman and Sanders, 1978; Wu et al., 2015). The characteristics of grain size can be expressed by the  
298 grain size distribution curve, and usually the mean or median diameter is used (Xu, 1999). In this study, the value of  
299 mean grain size ( $M_z$ ) showed that two major grain size boundaries occur at depths of 34 and 19 cm, separating a  
300 middle sedimentary unit (34–19 cm) that contains coarser sediment than the lower and upper sedimentary units that



301 contain finer sediment (Figure 6d). At these boundaries, the sand content changes from approximately 15.7% to 39.4%  
302 and then to 11.2% (Figure 6a), silt content changes from 59.7–82.1% to 51.5%–58.3% and then to 62.5–75.1% (Figure  
303 6b), and clay content changes from 16% to 5.8% and then to 19.8% in an upward direction (Figure 6c). On the basis of  
304  $^{137}\text{Cs}$  and  $^{210}\text{Pb}$  chronologies (Figure 2), we speculate that these significant changes of grain size parameters at depths  
305 of 34 and 17 cm might represent a record of the channel shifts of the YR in 1855 AD and 1976 AD, respectively.

306 The sediment of Laizhou Bay mainly comes from the YR and other small rivers located in the southern part of  
307 Laizhou Bay (Zhang et al., 2017; Gao et al., 2018). Prior to 1855 AD, when the YR entered the Yellow Sea, the  
308 sediments contribution to the BS of other small rivers was relatively larger. The fine fraction suspension sediment that  
309 was derived from other small rivers favors the hypothesis of fine sediment accumulation in core CJ06–435 during this  
310 period.

311 When the YR reentered the BS after 1855 AD, the dispersal of YR material contributed substantially to the  
312 sedimentation of the BS. It was reported that more than 80% of the YR sediment discharges into the BS during  
313 summer (Bi et al., 2011). Owing to the barrier effect of the tidal shear front and the weak river flow, most of the  
314 river-delivered sediment is deposited on the offshore delta within 15 km of the river mouth (Wang et al., 2007; Bi et al.,  
315 2010). Only a small part of the fine clay fraction is transported by the coastal currents over long distances and  
316 deposited across or along the shore in summer time (Wu et al., 2015). During the winter (October to March) season,  
317 the much stronger winter monsoon generate large waves, resulting in intensive sediment resuspension in the coastal  
318 region owing to the enhanced bottom shear stress (Yang et al., 2011; Bi et al., 2011). The resuspended sediment is  
319 transported southeastward along the coast of Laizhou Bay by the monsoon-enhanced coastal currents passing through  
320 the location of the sediment core CJ06–435. Therefore, after 1855 AD, the sediment of core CJ06–435 mainly included  
321 the fine fraction of the suspended sediment dispersed from the YR mouth, resuspended sediment from the coastal area  
322 off the YR delta in the winter, and locally resuspended sediment.

323 The accumulation of YR-suspended sediment during the summer season in Laizhou Bay was closely associated  
324 with the sediment dispersion pattern off the active delta lobe (Xing et al., 2016). The estuary of the YR, during most of  
325 the period 1855–1976 AD, was north of the modern YRD, and suspended sediment from the YR was transported



326 northeastward to Bohai Bay and the central Bohai basin. The contribution of YR-suspended sediment to the  
327 sedimentation of core CJ06–435 was smaller and the resuspended sediment became a dominant material source. Jiang  
328 and Wang (2005) found that the shapes of the sediment grain-size distributions in the YR mouth nearshore area are all  
329 characterized by bimodal curves with peaks near 1.2  $\mu\text{m}$  and 30–60  $\mu\text{m}$ . In the offshore area of Laizhou Bay, the  
330 sediment grain size is characterized by a mono-modal pattern, and most of the particles are concentrated at peaks near  
331 40–60  $\mu\text{m}$  (Jiang and Wang, 2005). During the winter, the large waves generated by the strong winds may result in  
332 intensive resuspension of the seabed sediment and lead to part of the coarse sediment in the YR mouth and Laizhou  
333 Bay being transported to the study area, which induces an evident increase in mean grain size and a decrease in the  
334 amount of fine grain sized particles. After 1976 AD, the lower channel of the YR shifted to the Qingshuigou course in  
335 Laizhou Bay; the suspended sediments derived from the YR estuary were primarily driven southward and  
336 southeastward along the coast, leading an increasing transportation of most of the YR-suspended sediment into  
337 Laizhou Bay (Qiao et al., 2010). As a result, the dispersal of river-laden sediment contributed substantially to the  
338 sedimentation of core CJ06–435, with a fine-grained layer being formed in the upper part of the core.

339 The results inferred from our grain-size data on the migrations of the YR lower channel since 1855 AD and their  
340 effects on the sedimentary environments of the adjacent BS have been proven by some studies from Laizhou Bay (Wu  
341 et al., 2015) and central BS (Hu et al., 2011). Based on the records of sediment core collected from Laizhou Bay, Wu et  
342 al. (2015) found that when the YR mouth approached the core location, the sediment became finer; otherwise, the  
343 active resuspension resulted in the accumulation of coarser sediment owing to strong hydrodynamics. The grain-size  
344 results from the central mud areas of the BS also point to the conclusion that the sediment supply from the YR to the  
345 central BS was cut off because of the shift of the YR terminal course from the Diaokou source in outer Bohai Bay to  
346 the Qingshuigou course in Laizhou Bay in 1976; hence, resuspended sediment became a primary source of sediment  
347 dispersal in the central BS. As a result, there was a significant increase in the proportion of sand in surface sediment in  
348 the central BS (Hu et al., 2011).

349 It is worth noting that the variation of grain size characteristics in the period of 6570–5000 a BP is very similar to  
350 that after 1855 AD. As shown in Figure 6d, the shift of Mz in the period of 6570–5000 a BP also began with a



351 significantly increased of Mz at 6570 a BP (160 cm) when the YR flowed into the BS in northern Shangdong province.  
352 This similar variation of grain size in the period of 6570-5000 a BP (superlobe 1) and after 1855 AD (superlobe 10) is  
353 likely implying a similar YR channel shifting during these two periods. However, more efforts are needed to reveal  
354 how the deltaic and neritic sea sedimentary environment was impacted by the river system.

355

### 356 **5.3. Coastal salt marsh response to hydrological change**

357 Two high-amplitude salt marsh vegetation shifts are displayed in the herb pollen record during 6570-5000 a BP  
358 (superlobe 1) and after 1855 AD (superlobe 10), indicating rapid oscillations of environmental conditions in the coastal  
359 area of BS. Within single intervals of the Yellow River superlobe, a recurrent and directional alternation of herb pollen  
360 taxa is observed in the following order: the shift of herb pollen data began with an abrupt decrease of Cyperaceae  
361 percentages, followed by a steep increase of Chenopodiaceae and *Artemisia* (Figure 7b).

362 Cyperaceae, Chenopodiaceae, and *Artemisia* are the three plant families/genus that contain the important  
363 representatives of coastal salt marsh plants (Lu et al., 2006). In the salt marsh of the modern YRD, species composition  
364 of Cyperaceae, Chenopodiaceae, and *Artemisia* varies with salinity and soil moisture. Plant families such  
365 as Cyperaceae are mainly composed of hydrophytes and phreatophyte *Heleocharis valliculosa*, *Cyperus rotundus*,  
366 *Scirpus planiculmis*, *S. triqueter*, *S. yagara*, *S. juncooides*, and *Juncellus serotinus* (Pan and Xu, 2011). The presence of  
367 Cyperaceae necessarily indicates lower saline conditions, since hydrophytes and phreatophyte sedges typically  
368 colonize in the middle and upper part of the supralittoral zone, both sides along the riverbank, the coast of the lake, and  
369 the interfluvial lowlands of the paleo-river. These areas are far from the coastline, and the main type of soil is salinized  
370 soil with lower salinity (Zhang et al., 2009a; Xu, 2011). Chenopodiaceae are mainly composed of halophyte *Suaeda*  
371 *glauca*, *S. salsa*, and *Salicornia europaea*. *Artemisia* mainly consist of halophyte and xerophyte *Artemisia carvifolia*, *A.*  
372 *capillaris*, and *A. annua* (Xing et al., 2003; Zhang et al., 2009b). In the modern YRD, halophyte is distributed in the  
373 intertidal zone mudflat and the outside margin part of the supralittoral zone. These areas are near the coastline,  
374 characterized by a high incidence of wave brakes and prolonged inundation regimes, and the main type of soil is saline  
375 (Zhang et al., 2009b). So, in salt marsh plant communities, the variation of Cyperaceae, Chenopodiaceae, and



376 *Artemisia* contents often thought to reflect environmental gradients controlled by the distance from the coast, local  
377 topography, terrigenous material and freshwater input (Gonza lez and Dupont, 2009; Zhang et al., 2009a). The pollen  
378 record from the BS could provide evidence of coastal salt marsh development over decade-to-century of years as a  
379 response to environmental alternations during the period of hydrological change.

380 In the studied sequence, the YR flowed into the BS towards the northern Shandong Province after a course shift.  
381 The lower river was initially braided upon relocation, as characterized by unchannelized river flow. At this initial stage,  
382 the river-derived sediment was largely accumulated in the floodplain and/or among the antecedent rivers owing to the  
383 lack of channelization (Wu et al., 2017), filling the coast of the lake, the interfluvial lowlands of the paleo-river, and  
384 the supralittoral zone, etc., causing the destruction of hydrophytes and phreatophyte sedges in these areas. This process  
385 is indicated in our records by the significant decrease of Cyperaceae pollen percentages shown for superlobe 1 and  
386 superlobe 10 (Figure 7b).

387 Eventually, natural channel adjustments resulted in the coalescence of multiple channels into a single channel  
388 (Wu et al., 2017). A large amount of river-derived sediment was deposited at the mouth of the YR, causing the  
389 progradation of the YRD. Upon the original formation of the intertidal zone in the YRD, it was a bare beach wetland,  
390 because of strongly influenced by tides. Along with the expansion of new forming beach wetland to migrate seaward,  
391 the influence of tides was weakening on the original bare beach wetland and the salinity of original beach wetland was  
392 decreasing (Zhang et al., 2007). Pioneer species of salt marshes, e.g., *S. glauca*, *S. salsa* and *Salicornia europaea*  
393 (Chenopodiaceae), first colonized this original bare beach wetland (Zhang et al., 2009a). The significant increase of  
394 Chenopodiaceae in our pollen record (Figure 7b) is therefore interpreted as the development of the *S. glauca*  
395 population.

396

#### 397 **5.4. Palaeovegetation reconstruction and its climate significance**

398 The palynofloral assemblages (Figure 3) can be used to trace the vegetation successions and climate change  
399 around the western BS. As shown in Figure 3 and 4, the vegetation went through six stages of successions.

400 Vegetation Stage 1 (8500–6500 a BP, 271–156 cm), the palynofloral assemblages are mainly composed of the



401 pollen of broad-leaved trees, such as *Quercus*, *Betula*, *Alnus*, and Ulmaceae, combined with those of  
402 hydrophytes and phreatophyte Cyperaceae and *Typha*, among which, the pollen of *Quercus* and *Typha* are predominant  
403 (Figure 3 and 4). In contrast, the pollen of halophytic and xerophytic herbs and conifer trees is scarce. The pollen  
404 results suggest that the land area of the western BS was dominated by broadleaved forest and freshwater wetlands,  
405 indicating a markedly warmer and wetter climate than the present. The highest values of AP pollen concentration  
406 (Figure 4), reflecting a dense vegetation cover, also represent warm conditions during this period. The pollen data are  
407 comparable to that found from previous palynological studies carried out in North China (e.g., Yi et al., 2003; Ren,  
408 2007; Chen and Wang, 2012; Sun and Feng, 2015; Hao et al., 2016; Wen et al., 2017) and Northeast China (e.g., Ren  
409 and Beug, 2002; Stebich et al., 2015), from which a warm, wet climate corresponding to the Holocene Optimum was  
410 inferred. The pollen assemblages encountered herein indicated that the vegetation of the Shandong Peninsula consisted  
411 mainly of broadleaved forest, with some conifer trees on the uplands, and freshwater lakes and marshes dominated the  
412 coastal area, under the influence of the Holocene climatic optimum.

413 Vegetation Stage 2a (6500–5900 a BP, 156–128 cm), a climatic cooling period is identified by an increase of  
414 conifers, *Pinus*, combined with an abrupt reduction of broadleaved trees. Halophytic and xerophytic herbs taxa such as  
415 Compositae, *Artemisia*, and Chenopodiaceae also increase, while Cyperaceae and aquatic herbs *Typha* obviously  
416 decrease. The climate shift from warm, wet to cool, and dry may have caused the reduction of broadleaved deciduous  
417 forests and the expansion of conifer forests, the freshwater lakes and marshes had spread over the coastal area of BS  
418 were gradually disappearing. As introduced in above, a vast imbrication delta complex began to build up at the western  
419 part of the BS after 6570 a BP, which resulted in the increase of land area and development of the YR delta wetland. It  
420 can be concluded that the expansion of saltbush during this period may be partly related to the formation of the YR  
421 delta complex.

422 Vegetation Stage 2b (5900–3500 a BP, 128–63 cm), the pollen data show that broadleaved trees such as *Quercus*,  
423 *Pterocarya*, Ulmaceae and Moraceae were fewer during this period, whereas halophytic and xerophytic herbs  
424 (*Artemisia* and Chenopodiaceae) increased (Figure 3 and 4) compared with the previous period. These associations  
425 may indicate cooler and drier climatic conditions.



426 Vegetation Stage 2c (3500–1000 a BP, 63–41 cm), a warm climatic phase occurred, as suggested by the increase  
427 in representatives of broadleaved trees (*Quercus*, *Betula*, *Alnus*, *Pterocarya*, and Ulmaceae), with low frequencies of  
428 conifer pollen (*Pinus*) throughout the interval. Moreover, halophytic and xerophytic herb pollen, including Compositae,  
429 *Artemisia*, and Chenopodiaceae, still occurred with high frequency (Figure 3 and 4). Accordingly, the assemblages  
430 reveal that a warm, dry climate probably developed during the late Holocene. Based on 73 selected globally distributed  
431 Holocene temperature records, Marcott et al. (2013) found a global mean temperature pattern with a warmer early and  
432 middle Holocene (ca. 10000–5000 a BP) followed by a long-term cooling trend towards the late Holocene. However,  
433 many Holocene temperature records from central Asia (Aizen et al., 2016; Huang et al., 2015; Rao et al., 2019), the  
434 Tibetan Plateau (Thompson et al., 1997; Zhao et al., 2013), and North China (Jiang et al., 2006) revealed an  
435 irreconcilable conflict with the synthesized record of Marcott et al. (2013). These records indicated a warm early  
436 Holocene from ca. 10000 to 7000–6000 a BP, a cold mid-Holocene from ca. 7000–6000 to 4000–3000 a BP, and then a  
437 warming late Holocene from ca. 3000–4000 a BP to the present, consistent with the basic change pattern of our  
438 temperature record.

439 Vegetation Stage 2d (1000 a BP–after 1855 AD, 41–30 cm), there is a dramatic decrease in the occurrence of  
440 *Quercus*, quickly followed by a sudden increase in *Pinus* (Figure 3 and 4). These pollen data suggest that the previous  
441 warm temperature deciduous broadleaved forests dominated by *Quercus* were replaced by secondary vegetation *Pinus*  
442 under anthropogenic influence. This assumption is supported by previous palynological studies. Yi et al. (2003) found  
443 a sudden reduction of *Quercus*, followed by a marked increase of *Pinus* after 1300 a BP at the YRD. Their research  
444 considered that this typical lag between the two taxa may indicate that, after the clearance of the local broadleaved  
445 deciduous forests, the vegetation was replaced by a secondary pine forest. Park and Kim (2015) also interpreted the  
446 decrease in the percentage of *Quercus* and increase of *Pinus* in the late Holocene as marking the development of  
447 secondary vegetation under anthropogenic influence.

448 Vegetation Stage 3 (after 1855 AD, 30–0 cm), a significant decline in broadleaved trees (*Quercus*) and conifers  
449 (*Pinus*) pollen, as well as an increase in the frequency of herbs (Poaceae, Compositae, *Artemisia*, and Chenopodiaceae)  
450 pollen may reflect the further strengthening of human disturbance on the vegetation and the expansion of intensive



451 agricultural cultivation into forests of the BS coastal area. Moreover, after 1855 AD, the present YR began returning to  
452 the BS, and forming a vast area of floodplain and estuarine wetland on the southwest coast of the BS (Saito et al., 2000;  
453 Jiang et al., 2013). The variation of herb pollen may be partly related to the development of the modern YRD wetland.

454

### 455 **5.5. Holocene temperature variations in North China and possible driving mechanisms**

456 As shown in Figure 8b, the *Quercus* pollen percentage of core CJ06-435, as a temperature index, exhibits a warm  
457 early Holocene from 8500 to 6500 a BP, a cool mid-Holocene from 6500 to 3500 a BP, and then a relatively warm late  
458 Holocene from 3500 to 1000 a BP. After 1000 a BP, the strengthening of human activity destroyed the natural  
459 vegetation of the study area, and the temperature could not be reconstructed by our pollen results. This temperature  
460 record is reasonably corroborated by four recently-published and relatively well-dated sequences from North China,  
461 Northwest China, and the Tibetan Plateau (see Figure 1a for site locations), including the sedimentary pollen-based  
462 temperature record from the Narenxia Peat within the Kanas Lake, Northwest China (Figure 8c; Feng et al., 2017); the  
463 Guliya ice core  $\delta^{18}\text{O}$  record from the western Kunlun Shan, southwestern Tibetan Plateau (Figure 8d; Thompson et al.,  
464 1997); alpine peat  $\alpha$ -cellulose  $\delta^{13}\text{C}$  record from the Altai Mountains in Northwest China (Figure 8e; Rao et al., 2019);  
465 and lacustrine sedimentary pollen-based quantitative temperature record (the mean annual temperature) from Lake  
466 Bayanchagan in Inner Mongolia in North China (Figure 8f; Jiang et al., 2006). All four records indicate that the  
467 temperature was high between 8500 and 6000 a BP, low between 6000 and 3000–4000 a BP, and averagely high during  
468 the past 3000–4000 a BP (Figure 8c–f), consistent with the basic change pattern of our pollen-based temperature index  
469 (Figure 8b). The comparison of the five records demonstrates that the CJ06-435 core *Quercus* pollen percentage record  
470 is, at a minimum, of regional significance.

471 Insolation has been widely accepted as an important factor in Holocene climate variation. The covariation of  
472 Northern Hemisphere extratropics (30 ° to 90 ° N) temperature and local summer insolation on an orbital scale, and the  
473 long-term decrease of summer insolation make the especially pronounced cooling of the Northern Hemisphere  
474 extratropics during the Holocene (Marcott et al., 2013) appear reasonable. However, the general pattern of temperature  
475 variation revealed by our study is not entirely consistent with local mean annual insolation forcing (Figure 8a). Our



476 results indicated a cold mid-Holocene from 6500 to 3500 a BP and a relatively warm late Holocene. This temperature  
477 characterization of a cool mid-Holocene and a relatively warm late-Holocene is also seen in many proxy records in the  
478 North and Northwest China (Thompson et al., 1997; Jiang et al., 2006; Aizen et al., 2016; Hou et al., 2016; Feng et al.,  
479 2017; Rao et al., 2019). Furthermore,  $\delta^{18}\text{O}$  data of permafrost ice wedges from the Lena River Delta in the Siberian  
480 Arctic reflect warming winter season temperature over the past 7000 years (Meyer et al., 2015). Therefore, forcings  
481 other than Northern Hemisphere insolation are required to explain the cooler mid-Holocene seen in the mid-high  
482 latitudes of continental Eurasia. Two such possible forcings are the changes in greenhouse gases (GHG) concentrations  
483 and variations of El Niño-Southern Oscillation (ENSO) activities.

484 Radiative forcing by GHG rose  $0.5 \text{ W/m}^2$  during the mid-late Holocene (Marcott et al., 2013), which would be  
485 expected to yield  $1^\circ \text{ C}$  warming at Kinderlinskaya Cave in the southern Ural Mountains from 7 ka to the pre-industrial  
486 (Baker et al., 2017). Recently, both winter insolation and GHG forcing have been proposed as the major driving factors  
487 for winter warming during the past 7 ka in the Siberian Arctic (Meyer et al., 2015) and the southern Ural Mountains  
488 (Baker et al., 2017). Similarly, summer warming in central Asia during the mid-late Holocene, recorded by the alpine  
489 peat  $\alpha$ -cellulose  $\delta^{13}\text{C}$  record from the Altai mountains (Rao et al., 2019), has been proposed to be mainly driven by the  
490 enhanced GHG forcing and strengthened human activities. Hence, it appears that GHG forcing is an important driver  
491 for mid-late Holocene temperature variations.

492 We compared our pollen-based temperature index (Figure 8b) with the frequency of El Niño events reconstructed  
493 from the Botryococcene concentration in the El Junco Lake sediment (Figure 8g; Zhang et al., 2014) and the ENSO  
494 variability reconstructed from  $\delta^{18}\text{O}$  values of individual planktonic foraminifera retrieved from deep-sea sediments  
495 (Figure 8h; Koutavas and Joanides, 2012). As shown in Figure 8, lower temperature periods in mid-Holocene tend to  
496 occur during a period of low El Niño activity, which indicates that some link may exist between the temperature of  
497 Shandong Peninsula and the ENSO system. Modern research suggested that ENSO can influence the evolution of  
498 temperature behavior (Triacca et al., 2014). In East Asia, the strength of winter monsoon and East Asia troughs  
499 weakens in an El Niño year, and the weakening could cause the observed winter half-year warming (Xu et al., 2005).  
500 At a millennial time scale, using pollen data from Lake Moon in the central part of the Great Khingan Mountain Range,



501 Wu et al. (2019) have recently connected increased El Niño frequency with the shrinkage of winter monsoon activity  
502 in the East Asia, and the warming of winter temperature in the Great Khingan Mountain Range since the mid-Holocene.  
503 Likewise, the results of this study, indicating more or less synchronicity of the climate change at Shandong Peninsula  
504 and ENSO activity, provide a possible linkage between North China climate and oceanic forcing during mid-late  
505 Holocene.

506 In summary, the temperature characterizations of a cool mid-Holocene and a relatively warm late-Holocene  
507 revealed by the mid-high latitudes of continental Eurasia records can be explained by the change of insolation, GHG  
508 forcing and ENSO activity. The cooler mid-Holocene may be related to a combination of the decreasing summer  
509 insolation, relatively lower GHG radiative forcing, and weak El Niño activity during this interval. Along with  
510 enhanced GHG forcing and strengthened ENSO activity in the late Holocene, there was increased temperature.

511

## 512 **6. Conclusions**

513 Through the palynological and grain size reconstruction of coastal area vegetation and environment in core  
514 CJ06–435, we were able to identify specific responses of plant communities to climatic (temperature, precipitation),  
515 hydrological (Y ) and anthropogenic impacts. Our data elucidate the pattern and mechanisms driving coastal salt  
516 marsh succession at decade-to-century timescales. Two intervals of expanded salt marsh vegetation correspond to the  
517 formation of Y ) delta superlobes, indicating that soil development and salinity gradients are the main factors  
518 determining the vegetation dynamics of coastal wetland. Our pollen-based temperature index revealed a warm early  
519 Holocene (8500–6500 a BP), a subsequent cool stage between 6500 and 3500 a BP, and a warm episode from 3500 to  
520 1000 a BP. The reliability of the record, especially the cooler mid-Holocene, is further supported by the other several  
521 temperature records from North China, Northwest China, and the Tibetan Plateau. We suggest that changes in  
522 insolation, GHG forcing, and ENSO activity could have played an important role in the temperature evolution at the  
523 mid-high latitudes of continental Eurasia.

524

525



526 **Code/Data availability**

527 The co-authors declare that all data included in this study are available upon request by contact with the  
528 corresponding author (Email: *jinxiachen@fio.org.cn*).

529

530

531 **Author contribution**

532 Jinxia Chen wrote the manuscript; Xuefa Shi and Yanguang Liu revised the manuscript many times; Shuqing  
533 Qiao provided many constructive suggestions for the manuscript, Shixiong Yang, Shijuan Yan, Huahua Lv, Xiaoyan Li  
534 and Chaoxin Li provided financial support for the collection of samples and obtained samples.

535

536

537 **Competing interests**

538 The authors declare that they have no conflict of interest.

539

540

541 **Acknowledgements**

542 We thank the shipboard teams of the R/V *Kan407* for sampling. We also thank Dr. Nan Qingyun for improving  
543 this paper. This work was supported by the National Natural Science Foundation of China (Grant Nos. 41420104005  
544 and 41576054).

545

546

547

548 **References**

549 Aizen, E.M., Aizen, V.B., Takeuchi, N., Mayewski, P.A., Grigholm, B., Joswiak, D.R., Nikitin, S.A., Fujita, K., Nakawo, M.,  
550 Zapf, A., Schwikowshi, M.: Abrupt and moderate climate changes in the mid-latitudes of Asia during the Holocene, J.



- 551 Glaciol., 62, 411–439, 2016.
- 552 Bao, R., Alonso, A., Delgado, C., Pagés, J.L.: Identification of the main driving mechanisms in the evolution of a small  
553 coastal wetland (Traba, Galicia, NW Spain) since its origin 5700 cal yr BP, *Palaeogeogr. Palaeoclimatol. Palaeoecol.*,  
554 247, 296–312, 2007.
- 555 Baker, J.L., Lachniet, M.S., Chervyatsova, O., Asmerom, Y. & Polyak, V.: Holocene warming in western continental Eurasia  
556 driven by glacial retreat and greenhouse forcing, *Nat. Geosci.*, <https://doi.org/10.1038/NGEO2953>, 2017.
- 557 Bi, N.S., Yang, Z.S., Wang, H.J., Hu, B.Q., Ji, Y.J.: Sediment dispersion pattern off the present Huanghe (Yellow River)  
558 subdelta and its dynamic mechanism during normal river discharge period, *Estuar. Coast. Shelf. S.*, 86, 352–362, 2010.
- 559 Bi, N.S., Yang, Z.S., Wang, H.J., Fan, D.J., Sun, X.X., Lei, K.: Seasonal variation of suspended-sediment transport through  
560 the southern Bohai Strait, *Estuar. Coast. Shelf. S.*, 93, 239–247, 2011.
- 561 Byun, J.G., Lee, W.K., Kim, M., Kwak, D.A., Kwak, H., Park, T., Byun, W.H., Son, Y., Choi, J.K., Lee, Y.J., Saborowski, J.,  
562 Chung, D.J., Jung, J.H.: Radial growth response of *Pinus densiflora* and *Quercus* spp. To topographic and climatic  
563 factors in South Korea, *J. Plant. Ecol.*, 6, 380–392, 2013.
- 564 Chen, J.X., Nan, Q.Y., Li, T.G., Sun, R.T., Sun, H.J., Lu, J.: Variations in the East Asian winter monsoon from 3500 to  
565 1300 cal. yr BP in northern China and their possible societal impacts, *J. Asian Earth Sci.*,  
566 <https://doi.org/10.1016/j.jseaes.2019.103912>, 2019a.
- 567 Chen, J.X., Li, T.G., Nan, Q.Y., Shi, X.F., Liu, Y.G., Jiang, B., Zou, J.J., Selvaraj, K., Li, D.L., Li, C.S.: Mid-late Holocene  
568 rainfall variation in Taiwan: A high-resolution multiproxy record unravels the dual influence of the Asian monsoon and  
569 ENSO, *Palaeogeogr. Palaeoclimatol. Palaeoecol.*, 516, 139–151, 2019b.
- 570 Chen, W., Wang, W.M.: Middle-Late Holocene vegetation history and environment changes revealed by pollen analysis of a  
571 core at Qingdao of Shandong Province, East China, *Quat. Int.*, 254, 68–72, 2012.
- 572 Cohen, M.C.L., Lara, R.J., Smith, C.B., Angélica, R.S., Dias, B.S., Pequeno, T.: Wetland dynamics of Marajó Island,  
573 northern Brazil, during the last 1000 years, *Catena*, 76(1), 70–77, 2008.
- 574 Cohen, M.C.L., Pessenda, L.C.R., Behling, H., Rossetti, D.d.F., França, M.C., Guimarães, J.T.F., Friaes, Y., Smith, C.B.:  
575 Holocene palaeoenvironmental history of the Amazonian mangrove belt, *Quat. Sci. Rev.*, 55, 50–58, 2012.
- 576 Cui, B.S., Yang, Q.C., Yang, Z.F., Zhang, K.J.: Evaluating the ecological performance of wetland restoration in the Yellow  
577 River Delta, China, *Ecol. Eng.* 35, 1090–1103. 2009.
- 578 Dai, L., Weng, C.Y., Lu, J., Mao, L.M.: Pollen quantitative distribution in marine and fluvial surface sediments from the  
579 northern South China Sea: new insights into pollen transportation and deposition mechanisms, *Quat. Int.*, 325, 136–149,  
580 2014.
- 581 Dai, L., Weng, C.Y.: Marine palynological record for tropical climate variations since the late last glacial maximum in the  
582 northern South China Sea, *Deep-sea. Res. Pt. II.*, 122, 153–162, 2015.
- 583 Engelhart, S.E., Horton, B.P., Roberts, D.H., Bryant, C.L., Corbett, D.R.: Mangrove pollen of Indonesia and its suitability as  
584 a sea-level indicator, *Mar. Geol.*, 242, 65–81, 2007.
- 585 Feng, Z.D., Sun, A.Z., Abdusalih, N., Ran, M., Kurban, A., Lan, B., Zhang, D.L., Yang, Y.P.: Vegetation changes and  
586 associated climatic changes in the southern Altai Mountains within China during the Holocene, *Holocene*, 27(5), 683–  
587 693, 2017.



- 588 França, M.C., Francisquini, M.I., Cohen, M.C.L., Pessenda, L.C.R., Rossetti, D.F., Guimarães, J.T.F., Smith, C.B.: The last  
589 mangroves of Marajó Island–Eastern Amazon: Impact of climate and/or relative sea-level changes, *Rev. Palaeobot.*  
590 *Palyno.*, 187, 50–65, 2012.
- 591 França, M.C., Alves, I.C.C., Castro, D.F., Cohen, M.C.L., Rossetti, D.F., Pessenda, L.C.R., Lorente, F.L., Fontes, N.A.,  
592 Junior, A.Á.B., Giannini, P.C.F., Francisquini, M.I.: A multi-proxy evidence for the transition from estuarine mangroves  
593 to deltaic freshwater marshes, Southeastern Brazil, due to climatic and sea-level changes during the late Holocene,  
594 *Catena*, 128, 155–166, 2015.
- 595 Friedman, G.M., Sanders, J.E.: *Principles of sedimentology*, John Wiley and Sons, Inc, 1–792, 1978.
- 596 Gail, L.C., Alexei, S., Ian, D.C.: Pollen transport through distributaries and depositional patterns in coastal waters,  
597 *Palaeogeogr. Palaeoclimatol. Palaeoecol.*, 149, 257–270, 1999.
- 598 Gao, M.S., Guo, F., Hou, G.H., Qiu, J.D., Kong, X.H., Liu, S., Huang, X.Y., Zhuang, H.H.: The evolution of sedimentary  
599 environment since late Pleistocene in Laizhou Bay, Bohai Sea, *Geol. Chin.*, 45(1), 59–68, 2018. (in Chinese with  
600 English abstract)
- 601 Giraldo-Giraldo, M.J., Velásquez-Ruiz, C.A., Pardo-Trujillo, A.: Late-Holocene pollen-based paleoenvironmental  
602 reconstruction of the El Triunfo wetland, Los Nevados National Park (Central Cordillera of Colombia), *Holocene*, 28(2),  
603 183–194, 2018.
- 604 Gonza lez, C., Dupont, L.M.: Tropical salt marsh succession as sea-level indicator during Heinrich events, *Quat. Sci. Rev.*,  
605 28, 939–946, 2009.
- 606 Gu, Y.H., Xiu, R.C.: On the current and storm flow in the Bohai Sea and their role in transporting deposited silt of the Yellow  
607 River, *J. Oceanogr. Huanghai & Bohai Seas.*, 14(1), 1–6, 1996.
- 608 Hao, Q., Liu, H.Y., Liu, X.: Pollen-detected altitudinal migration of forests during the Holocene in the mountainous forest–  
609 steppe ecotone in northern China, *Palaeogeogr. Palaeoclimatol. Palaeoecol.*, 446, 70–77, 2016.
- 610 He, L., Xue, C.T., Ye, S.Y., Amorosi, A., Yuan, H.M., Yang, S.X., Laws, E.A.: New evidence on the spatial-temporal  
611 distribution of superlobes in the Yellow River Delta Complex, *Quat. Sci. Rev.*, 214, 117–138, 2019.
- 612 Hemavathi, S., Manjula, R., Ponmani, N.: Numerical Modelling and Experimental Investigation on the Effect of Wave  
613 Attenuation Due to Coastal Vegetation, *Proceedings of the Fourth International Conference in Ocean Engineering*  
614 (ICOE2018), 23, 99–110, 2019.
- 615 Hendy, I.L., Minckley, T.A., Whitlock, C.: Eastern tropical Pacific vegetation response to rapid climate change and sea level  
616 rise: A new pollen record from the Gulf of Tehuantepec, southern Mexico, *Quat. Sci. Rev.*, 145, 152–160, 2016.
- 617 Hou, J.Z., Huang, Y.S., Zhao, J.T., Liu, Z.H., Colman, S., An, Z.S.: Large Holocene summer temperature oscillations and  
618 impact on the peopling of the northeastern Tibetan Plateau, *Geophys. Res. Lett.*, 43, 1323–1330, 2016.
- 619 Hou, W., Hou, X.Y.: Spatial–temporal changes in vegetation coverage in the global coastal zone based on GIMMS NDVI3g  
620 data, *Int. J. Remote. Sens.*, 41(3), 1118–1138, 2020.
- 621 Hu, L.M., Guo, Z.G., Shi, X.F., Qin, Y.W., Lei, K., Zhang, G.: Temporal trends of aliphatic and polyaromatic hydrocarbons  
622 in the Bohai Sea, China: Evidence from the sedimentary record, *Org. Geochem.*, 42, 1181–1193, 2011.
- 623 Huang, D.J., Su, J.L., Backhaus, J.O.: Modelling the seasonal thermal stratification and baroclinic circulation in the Bohai  
624 Sea, *Cont. Shelf. Res.*, 19, 1485–1505, 1999.



- 625 Huang, X.Z., Chen, C.Z., Jia, W.N., An, C.B., Zhou, A.F., Zhang, J.W., Jin, M., Xia, D.S., Chen, F.H., Grimm, E.C.:  
626 Vegetation and climate history reconstructed from an alpine lake in central Tianshan Mountains since 8.5 ka BP,  
627 *Palaeogeogr. Palaeoclimatol. Palaeoecol.*, 432, 36–48, 2015.
- 628 Jiang, W.S., Wang, H.J.: Distribution of suspended matter and its relationship with sediment particle size in Laizhou Bay,  
629 *Oceanol. Limnol. Sin.*, 36(2), 97–103, 2005.
- 630 Jiang, W.Y., Guo, Z.T., Sun, X.J., Wu, H.B., Chu, G.Q., Yuan, B.Y., Hatte, C., Guiot, J.: Reconstruction of climate and  
631 vegetation changes of Lake Bayanchagan (Inner Mongolia): Holocene variability of the east Asian monsoon, *Quat. Res.*,  
632 65, 411–420, 2006.
- 633 Jiang, D.J., Fu, X.F., Wang, K.: Vegetation dynamics and their response to freshwater inflow and climate variables in the  
634 Yellow River Delta, China, *Quat. Int.*, 304, 75–84, 2013.
- 635 Kim, C., Park, J.H., Jang, D.H.: Changes of the forest types by climate changes using satellite imagery and forest statistical  
636 data: a case in the Chungnam Coastal Area, Korea, *J. Environ. Impact. Asses.*, 20, 523–538, 2011.
- 637 Kirchner, G., Ehlers, H.: Sediment Geochronology in Changing Coastal Environments: Potentials and Limitations of the  
638  $^{137}\text{Cs}$  and  $^{210}\text{Pb}$  Methods, *J. Coast. Res.*, 14, 483–492, 1998.
- 639 Korea Forest Service: Statistical Yearbook of Forestry. Daejeon, Korea: KFS, 2011.
- 640 Koutavas, A., Joanides, S.: El Niño–Southern Oscillation extrema in the Holocene and Last Glacial Maximum,  
641 *Paleoceanography*, <https://doi.org/10.1029/2012PA002378>, 2012.
- 642 Li, C.Y., Yan, L.Q., Han, T.X.: Research on composition of wetland vegetation in Shandong, *Shandong Forest Sci. Tech.*, 4,  
643 27–29, 2007. (in Chinese with English abstract)
- 644 Liu, W.Z., Zhang Q.F., Liu, G.H.: Seed banks of a river–reservoir wetland system and their implications for vegetation  
645 development, *Aquat. Bot.*, 90, 7–12, 2009.
- 646 Liu, D.Y., Li, X., Emeis, K.C., Wang, Y.J., Richard, P.: Distribution and sources of organic matter in surface sediments of  
647 Bohai Sea near the Yellow River Estuary, China, *Estuar. Coast. Shelf. S.*, 165, 128–136, 2015.
- 648 Lu, J.J., He, W.S., Tong, C.F., Wang, W.: *Wetland Ecology*. Higher Education Press, Beijing, 2006.
- 649 Luo, C.X., Chen, M.H., Xiang, R., Liu, J.G., Zhang, L.L., Lu, J., Yang, M.X.: Characteristics of modern pollen distribution  
650 in surface sediment samples for the northern South China Sea from three transects, *Quat. Int.*, 286, 148–158, 2013.
- 651 Luo, C.X., Chen, M.H., Xiang, R., Liu, J.G., Zhang, L.L., Lu, J., Yang, M.X.: Modern pollen distribution in marine  
652 sediments from the northern part of the South China Sea, *Mar. Micropaleontol.*, 108, 41–56, 2014.
- 653 Marcott, S.A., Shakun, J.D., Clark, P.U., Mix, A.C.: A reconstruction of regional and global temperature for the past 11,300  
654 years, *Science*, 339, 1198–1201, 2013.
- 655 Meyer, H., Opel, T., Laepple, T., Dereviagin, A.Y., Hoffmann, K., Werner, M.: Long-term winter warming trend in the  
656 Siberian Arctic during the mid- to late Holocene, *Nat. Geosci.*, <https://doi.org/10.1038/NGEO2349>, 2015.
- 657 Milliman, J.D., Meade, R.H.: World-wide delivery of river sediment to oceans, *J. Geol.*, 91, 1–21, 1983.
- 658 Milliman, J.D., Qin, Y.S., Ren, M.E., Saito, Y.: Man's influence on the erosion and transport of sediment by Asian rivers: the  
659 Yellow River (Huanghe) example, *J. Geol.*, 95, 751–762, 1987.
- 660 Montade, V., Nebout, N.C., Kissel, C., Mulsow, S.: Pollen distribution in marine surface sediments from Chilean Patagonia,  
661 *Mar. Geol.*, 282, 161–168, 2011.



- 662 Neumann, F.H., Scott, L., Bousman, C.B., As, L.V.: A Holocene sequence of vegetation change at Lake Eteza, coastal  
663 KwaZulu-Natal, South Africa, *Rev. Palaeobot. Palynol.*, 162, 39–53, 2010.
- 664 Pan, Y., Xu, J.W.: Studies on Resource and Flora of Aquatic Vascular Plants in Wetland of Yellow River Delta, *J. Anhui Agr.*  
665 *Sci.*, 39(3), 1642–1644, 2011. (in Chinese with English abstract)
- 666 Palinkas, C.M., Nittrouer, C.A.: Modern sediment accumulation on the Po shelf, Adriatic Sea, *Cont. Shelf Res.*, 27, 489–505,  
667 2007.
- 668 Park, J., Kim, M.: Pollen-inferred late Holocene agricultural developments in the vicinity of Woljeong-ri, southwestern  
669 Korea, *Quat. Int.*, 384, 13–21, 2015.
- 670 Pessenda, L.C.R., Vidotto, E., Oliveira, P.E.D., Jr, A.A.B., Cohen, M.C.L., Rossetti, D.d.F., Ricardi-Branco, F., Bendassolli,  
671 J.A.: Late Quaternary vegetation and coastal environmental changes at Ilha do Cardoso mangrove, southeastern Brazil.  
672 *Palaeogeogr. Palaeoclimatol. Palaeoecol.*, 363–364, 57–68, 2012.
- 673 Qiao, S.Q., Shi, X.F., Zhu, A.M., Liu, Y.G., Bi N.S., Fang, X.S., Yang, G.: Distribution and transport of suspended sediments  
674 off the Yellow River (Huanghe) mouth and the nearby Bohai Sea, *Estuar. Coast. Shelf. S.*, 86, 337–344, 2010.
- 675 Rao, Z.G., Huang, C., Xie, L.H., Shi, F.X., Zhao, Y., Cao, J.T., Gou, X.H., Chen, J.H., Chen, F.H.: Long-term summer  
676 warming trend during the Holocene in central Asia indicated by alpine peat  $\alpha$ -cellulose  $\delta^{13}\text{C}$  record, *Quat. Sci. Rev.*, 203,  
677 56–67, 2019.
- 678 Ren, G.Y., Beug, H.J.: Mapping Holocene pollen data and vegetation of China, *Quat. Sci. Rev.*, 21, 1395–1422, 2002.
- 679 Ren, G.Y.: Changes in forest cover in China during the Holocene, *Veget. Hist. Archaeobot.*, 16, 119–126, 2007.
- 680 Saito, Y., Wei, H.L., Zhou, Y.Q., Nishimura, A., Sato, Y., Yokota, S.: Delta progradation and chenier formation in the  
681 Huanghe (Yellow River) delta, China, *J. Asian Earth Sci.*, 18, 489–497, 2000.
- 682 Sander, V.D.K.: Pollen distribution in marine sediments from the south-eastern Indonesian waters, *Palaeogeogr.*  
683 *Palaeoclimatol. Palaeoecol.*, 171, 341–361, 2001.
- 684 Serrano, O., Lovelock, C.E., Atwood, T.B., Macreadie, P.I., Canto, R., Phinn, S., Arias-Ortiz, A., Bai, L., Baldock, J., Bedulli,  
685 C., et al.: Australian vegetated coastal ecosystems as global hotspots for climate change mitigation, *Nat. Commun.*,  
686 <https://doi.org/10.1038/s41467-019-12176-8>, 2019.
- 687 Spivak, A.C., Sanderman, J., Bowen, J.L., Canuel, E.A., Hopkinson, C.S.: Global-change controls on soil-carbon  
688 accumulation and loss in coastal vegetated ecosystems, *Nat. Geosci.*, 12, 685–692, 2019.
- 689 Sun, A.Z., Feng, Z.D.: Climatic changes in the western part of the Chinese Loess Plateau during the Last Deglacial and the  
690 Holocene: A synthesis of pollen records, *Quat. Int.*, 372, 130–141, 2015.
- 691 Stebich, M., Rehfeld, K., Schlütz, F., Tarasov, P.E., Liu, J.Q., Mingram, J.: Holocene vegetation and climate dynamics of NE  
692 China based on the pollen record from Sihailongwan Maar Lake, *Quat. Sci. Rev.*, 124, 275–289, 2015.
- 693 Stuiver, M., Reimer, P.J., Reimer, R.W.: CALIB 7.1 [WWW program, <http://calib.org>], 2019.
- 694 Thompson, L.G., Yao, T.D., Davis, M.E., Henderson, K.A., Mosley-Thompson, E., Lin, P.N., Beer, J., Synal, H.-A.,  
695 Cole-Dai, J., Bolzan, J.F.: Tropical climate instability: the last glacial cycle from a Qinghai-Tibetan ice core, *Science*,  
696 276, 1821–1825, 1997.
- 697 Triacca, U., Pasini, A., Attanasio, A., Giovannelli, A., Lippi, M.: Clarifying the Roles of Greenhouse Gases and ENSO in  
698 Recent Global Warming through Their Prediction Performance, *J. Clim.*, 27, 7903–7910, 2014.



- 699 Wang, K.F. and others: Spore-pollen and algal assemblages in the sediments of the Bohai Sea and palaeoenvironments.  
700 Geological Publishing House, Beijing, 1993.
- 701 Wang, H., Yang, Z., Li, Y., Guo, Z., Sun, X., Wang, Y.: Dispersal pattern of suspended sediment in the shear frontal zone off  
702 the Huanghe (Yellow River) mouth, *Cont. Shelf Res.*, 27, 854–871, 2007.
- 703 Wang, H.J., Wang, A.M., Bi, N.S., Zeng, X.M., Xiao, H.H.: Seasonal distribution of suspended sediment in the Bohai Sea,  
704 China, *Cont. Shelf Res.*, 90, 17–32, 2014.
- 705 Wen, R.L., Xiao, J.L., Fan, J.W., Zhang, S.R., Yamagata, H.: Pollen evidence for a mid-Holocene East Asian summer  
706 monsoon maximum in northern China, *Quat. Sci. Rev.*, 176, 29–35, 2017.
- 707 Woodroffe, S.A., Long, A.J., Milne, G.A., Bryant, C.L., Thomas, A.L.: New constraints on late Holocene eustatic sea-level  
708 changes from Mahe, Seychelles, *Quat. Sci. Rev.*, 115, 1–16, 2015.
- 709 Wu, X., Bi, N.S., Kanai, Y., Saito, Y., Zhang, Y., Yang, Z.S., Fan, D.J., Wang, H.J.: Sedimentary records off the modern  
710 Huanghe (Yellow River) delta and their response to deltaic river channel shifts over the last 200 years, *J. Asian Earth  
711 Sci.*, 108, 68–80, 2015.
- 712 Wu, X., Bi, N.S., Xu, J.P., Nittrouer, J.A., Yang, Z.S., Saito, Y., Wang, H.J.: Stepwise morphological evolution of the active  
713 Yellow River (Huanghe) delta lobe (1976–2013): Dominant roles of riverine discharge and sediment grain size,  
714 *Geomorphology*, <https://doi.org/10.1016/j.geomorph.2017.04.042>, 2017.
- 715 Wu, J., Liu, Q., Cui, Q. Y., Xu, D. K., Wang, L., Shen, C. M., Chu, G.Q., Liu, J.Q.: Shrinkage of East Asia winter monsoon  
716 associated with increased ENSO events since the mid-Holocene, *J. Geophys. Res.*, 124, 3839–3848, 2019.
- 717 Xing, S.Y., Xi, J.B., Zhang, J.F., Song, Y.M., Ma, B.Y.: The basic characteristics and the main types of vegetation in the  
718 Yellow River delta region, *J. Northeast Forest. Univ.*, 31(6), 85–86, 2003. (in Chinese)
- 719 Xing, G.P., Wang, H.J., Yang, Z.S., Bi, N.S.: Spatial and temporal variation in erosion and accumulation of the subaqueous  
720 Yellow River delta (1976–2004), *J. Coast. Res.*, 74, 32–47, 2016.
- 721 Xu, J.X.: Grain-size characteristics of suspended sediment in the Yellow River, China, *Catena*, 38, 243–263, 1999.
- 722 Xu, W.C., Ma, J.s., Wang, W.: A review of studys on the influence of ENSO events on the climate in China, *Sci. Meteorol.  
723 Sin.*, 25(2), 212–220, 2005.
- 724 Xu, Z.J., Zhang, X.L., Zhang, Z.H., Zhang, W.: Analysis of the biodiversity characters of coastal wetlands in southern  
725 Laizhou Bay, *Ecol. Env. Sci.*, 19(2), 367–372, 2010. (in Chinese with English abstract)
- 726 Xu, J.W.: Research on Diversity of Aquatic Vascular Plants in Wetland of Yellow River Delta, *Heilongjiang Agr. Sci.*, 1, 36–  
727 38, 2011. (in Chinese with English abstract)
- 728 Xue, C.T., Cheng, G.D.: Shelly ridges in west coast of Bohai Sea and Holocene Yellow River Delta system. In: Yang, Z.G.,  
729 Lin, H.M. (Eds.), *Quaternary Processes and Events in China Offshore and Onshore Areas*. China Ocean Press, Beijing,  
730 1989. (in Chinese with English abstract)
- 731 Xue, C.T.: Historical changes in the Yellow River delta, China, *Mar. Geol.*, 113, 321–329, 1993.
- 732 Xue, C.T., Zhu, X.H., Lin, H.M.: Holocene sedimentary sequence, foraminifera and ostracoda in west coastal lowland of  
733 Bohai Sea, China, *Quat. Sci. Rev.*, 14, 521–530, 1995.
- 734 Yang, Z.S., Ji, Y.J., Bi, N.S., Lei, K., Wang, H.J.: Sediment transport off the Huanghe (Yellow River) delta and in the  
735 adjacent Bohai Sea in winter and seasonal comparison, *Estuar. Coast. Shelf. S.*, 93, 173–181, 2011.



- 736 Yang, S.X., Li, J., Mao, L.M., Liu, K., Gao, M.S., Ye, S.Y., Yi, S., Zhou, L.Y., Wang, F.F.: Assessing pollen distribution  
737 patterns and provenance based on palynological investigation on surface sediments from Laizhou Bay, China: an aid to  
738 palaeoecological interpretation, *Palaeogeogr. Palaeoclimatol. Palaeoecol.*, 457, 209–220, 2016.
- 739 Yao, Z.Q., Shi, X.F., Li, X.Y., Liu, Y.G., Liu, J., Qiao, S.Q., Bai, Y.Z., Wang, X., Zhu, A.M., Wang, X.C.: Sedimentary  
740 environment and paleo-tidal evolution of the eastern Bohai Sea, China since the last glaciatio, *Quat. Int.*, 440, 129–138,  
741 2017.
- 742 Yi, S., Saito, Y., Oshima, H., Zhou, Y.Q., Wei, H.L.: Holocene environmental history inferred from pollen assemblages in the  
743 Huanghe (Yellow River) delta, China: climatic change and human impact, *Quat. Sci. Rev.*, 22, 609–628, 2003.
- 744 Zhang, G.S., Wang, R.Q., Song, B.M.: Plant community succession in modern Yellow River Delta, China, *J. Zhejiang Univ.*  
745 *Sci.*, 8(8), 540–548, 2007.
- 746 Zhang, X.L., Ye, S.Y., Yin, P., Chen, D.J.: Characters and successions of natural wetland vegetation in Yellow River Delta,  
747 *Ecol. Env. Sci.*, 18(1), 292–298, 2009a. (in Chinese with English abstract)
- 748 Zhang, X.L., Ye, S.Y., Yin, P., Yuan, H.M.: Flora characteristics of vascular plants of coastal wetlands in Yellow River Delta,  
749 *Ecol. Env. Sci.*, 18(2), 600–607, 2009b. (in Chinese with English abstract)
- 750 Zhang, Z.H., Leduc, G., Sachs, J.P.: El Niño evolution during the Holocene revealed by a biomarker rain gauge in the  
751 Gal ápagos Islands, *Earth Planet. Sci. Lett.*, 404, 420–434, 2014.
- 752 Zhang, P., Hu, R.J., Zhu, L.H., Wang, P., Yin, D.X., Zhang, L.J.: Distributions and contamination assessment of heavy metals  
753 in the surface sediments of western Laizhou Bay: Implications for the sources and influencing factors, *Mar. Pollut. Bull.*,  
754 <https://doi.org/10.1016/j.marpolbul.2017.03.046>, 2017.
- 755 Zhang, H.X., Zhang, M.L., Xu, T.P., Tang, J.: Numerical Investigations of Tsunami Run-Up and Flow Structure on Coastal  
756 Vegetated Beaches, *Water*, <https://doi.org/10.3390/w10121776>, 2018.
- 757 Zhao, C., Liu, Z.H., Rohling, E.J., Yu, Z.C., Liu, W.G., He, Y.X., Zhao, Y., Chen, F.H.: Holocene temperature fluctuations in  
758 the northern Tibetan Plateau, *Quat. Res.*, 80, 55–65, 2013.
- 759 Zheng, Z., Yang, S.X., Deng, Y., Huang, K.Y., Wei, J.H., Berne, S., Suc, J.P.: Pollen record of the past 60 ka BP in the  
760 Middle Okinawa Trough: Terrestrial provenance and reconstruction of the paleoenvironment, *Palaeogeogr.*  
761 *Palaeoclimatol. Palaeoecol.*, 307, 285–300, 2011.
- 762 Zhou, L.Y., Liu, J., Saito, Y., Gao, M.S., Diao, S.B., Qiu, J.D., Pei, S.F.: Modern sediment characteristics and accumulation  
763 rates from the delta front to prodelta of the Yellow River (Huanghe), *Geo-Mar. Lett.*, 36, 247–258, 2016.
- 764 Zhou, Z., Bian, C., Wang, C., Jiang, W., Bi, R.: Quantitative assessment on multiple timescale features and dynamics of sea  
765 surface suspended sediment concentration using remote sensing data, *J. Geophys. Res-Oceans.*, 122, 8739–8752, 2017.

766  
767  
768  
769  
770



771 **Table captions**

772

773 **Table 1:** AMS radiocarbon dates from core CJ06-435 and one tie points corresponding to the deepest onset of  $^{137}\text{Cs}$  in  
774 environmental samples at measurable levels; for calibration in years before present (a BP) 0 = 1950 AD.

775

776

777

Core depth (cm)	Materials	Radiocarbon date (a)	Age error (a)	Calibrated age (1 $\sigma$ ) (a BP)	Mean calibrated age (a BP)	Laboratory
25	$^{137}\text{Cs}$	–	–	–	–4	NIGLAS
7	Mixed foraminifera	3020	30	2854-3039	2951	Beta
13	Mixed foraminifera	2990	30	2817-2997	2913	Beta
17	Mixed foraminifera	3060	30	2908-3102	3003	WHOI
59	Mixed foraminifera	3340	30	3270-3485	3359	Beta
69	Mixed foraminifera	3590	25	3563-3725	3656	WHOI
87	Mixed foraminifera	4450	30	4695-4878	4801	Beta
119	Mixed foraminifera	5200	30	4812-4965	5706	WHOI
129	Mixed foraminifera	4520	30	4812-4965	4894	Beta
161	Mixed foraminifera	6020	30	6501-6667	6592	WHOI
183	Mixed foraminifera	6340	35	6886-7081	6981	WHOI

778 **Table 1**

779 AMS radiocarbon dates from core CJ06-435 and one tie points corresponding to the deepest onset of  $^{137}\text{Cs}$  in environmental  
780 samples at measurable levels; for calibration in years before present (a BP) 0 = 1950 AD.

781

782

783

784

785

786

787

788



789 **Figure caption**

790

791 **Figure 1:** (a) Locations of core CJ06-435 (red circle) and other sites referred to in this study (blue circles): ①  
792 Bayanchagan Lake (Jiang et al., 2006), ② Guliya ice core (Thompson et al., 1997), ③ Sahara sand wetland (Rao et  
793 al., 2019), ④ Narenxia Peat (Feng et al., 2017). (b) Topography and circulation of the study area. Circulation pattern  
794 (modified from Yao et al., 2017) is indicated by the black (winter), red (summer) and green (both summer and winter)  
795 arrows. YSWC: Yellow Sea Warm Current; LCC: Liaonan Coastal Current; BSCC: Bohai Sea Coastal Current.

796

797

798 **Figure 2:** Lithology, grain size, color reflectance  $L^*$  and  $a^*$ , magnetic susceptibility, and activity profiles for  $^{137}\text{Cs}$  and  
799  $^{210}\text{Pb}$  of core CJ06-435.

800

801

802 **Figure 3:** Percentage diagram of the principal pollen taxa from core CJ06-435. Pollen zonation is based on CONISS  
803 results.

804

805

806 **Figure 4:** Concentration diagram of the principal pollen taxa from core CJ06-435.

807

808

809 **Figure 5:** Spatial distribution of modern pollen percentage (black solid circle, %) and concentration (red open circle,  
810 grains/g) in Laizhou Bay, Bohai Sea (modified from Yang et al., 2016).

811

812

813 **Figure 6:** (a-f) Vertical profiles of grain-size parameters and halophytic and xerophytic herb (*Chenopodiaceae* and  
814 *Artemisia*) pollen percentage and concentration of core CJ06-435 ( $M_z$  – mean grain size). (g) The location of Yellow  
815 River superlobe 1 (Lijin superlobe) and superlobe 10 (Modern superlobe) (modified after Xue, 1993).

816

817

818 **Figure 7:** (a) Correlating proxy to paleo-superlobe variation of the YR, from top to bottom: percentage of *Cyperaceae*,  
819 *Chenopodiaceae*, and *Artemisia* pollen; concentration of *Chenopodiaceae*, *Artemisia*, and *Cyperaceae* pollen; sand  
820 percentage. (b) Detailed pollen and grain size profiles representing salt marsh species (*Cyperaceae*, *Chenopodiaceae*,  
821 *Artemisia*) relative abundances and hydrodynamic change during the formation of Yellow River superlobe 1 and 10.  
822 Pollen percentage of *Cyperaceae*, *Chenopodiaceae* and *Artemisia* from core CJ06-435 indicating the directional  
823 alternation of salt marshes along the Bohai Sea, ①— Unchannelized river flow characterized the onset of Yellow  
824 River channel shift, caused a large amount of river-derived sediment accumulation in the floodplain and destroyed  
825 the sedges in the coastal depression; ②—Along with the formation of a new channel, lateral migration of the lower



826 channel stopped, and new intertidal mudflat was formed. Pioneer species (*Chenopodiaceae*, *Artemisia*) first colonize  
827 bare zones of lower and middle marsh areas.

828  
829

830 **Figure 8:** Comparison of relevant Holocene temperature records (locations of the sites where the records are derived  
831 are illustrated in Fig. 1a) with solar irradiance and ENSO proxy records derived from the eastern equatorial Pacific. (a)  
832 Summer (mean of June) insolation irradiance for the Northern Hemisphere (40°N). (b) *Quercus* pollen percentage  
833 record from core CJ06-435, bold-red line is the five-point running average. (c) Pollen-based mean annual temperature  
834 (MAT) record from Narenxia Peat in the southern Altai (Feng et al., 2017). (d)  $\delta^{18}\text{O}$  record from the Guliya ice core in  
835 the western Kunlun Shan (Thompson et al., 1997). (e) Alpine peat  $\alpha$ -cellulose  $\delta^{13}\text{C}$  record from the Altai Mountains in  
836 central Asia (Rao et al., 2019). (f) Pollen-based mean annual temperature record from Lake Bayanchagan in Inner  
837 Mongolia, North China (Jiang et al., 2006). (g) Botryococcene concentrations in the El Junco sediment, a proxy for  
838 frequency of El Niño events (Zhang et al., 2014). (h) Variance of  $\delta^{18}\text{O}$  values of individual planktonic foraminifera (*G.*  
839 *ruber*) in sediment core V21–30 from the Galápagos region, a proxy for ENSO variance (Koutavas and Joanides, 2012).

840  
841

842

843

844

845

846

847

848

849

850

851

852

853

854

855





**Figure 2**

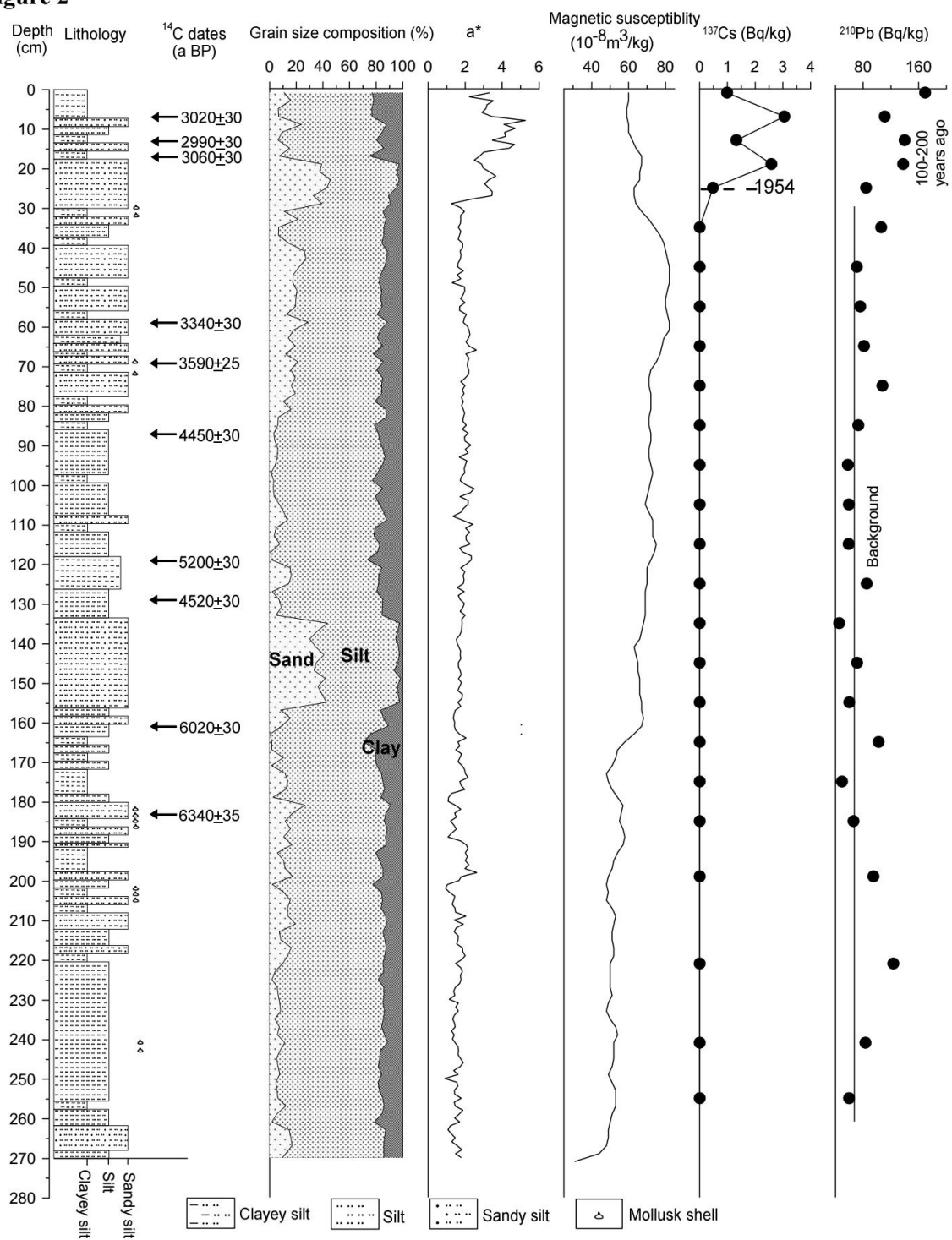




Figure 3

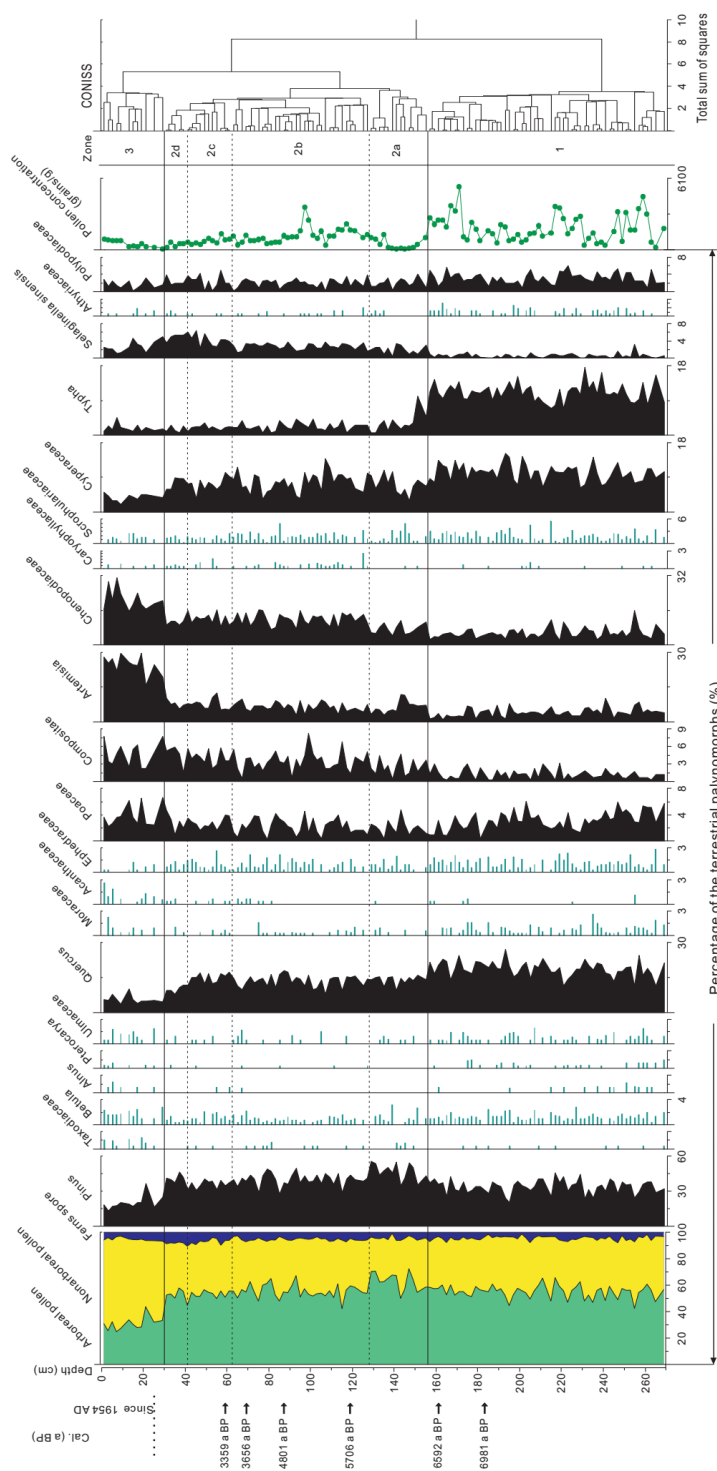




Figure 4

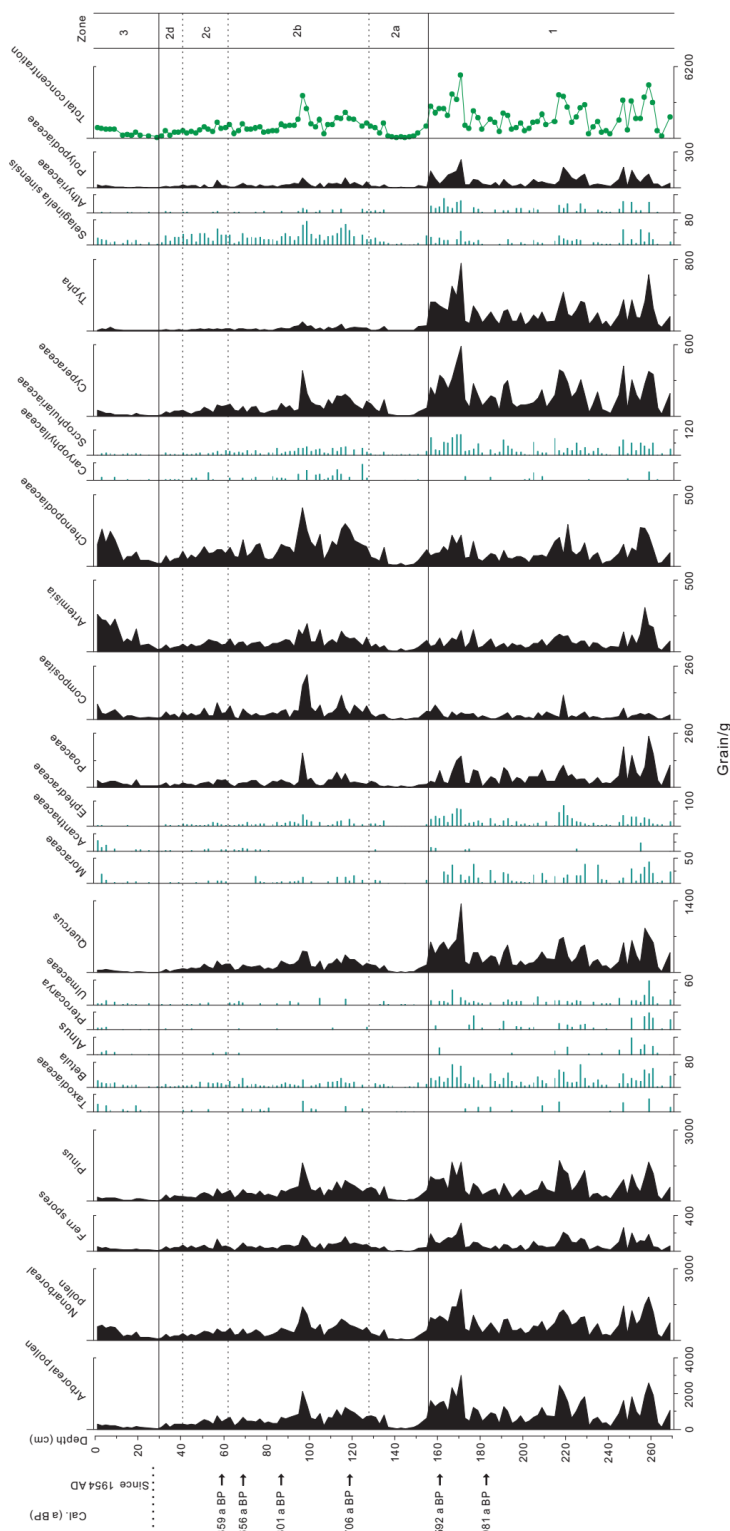
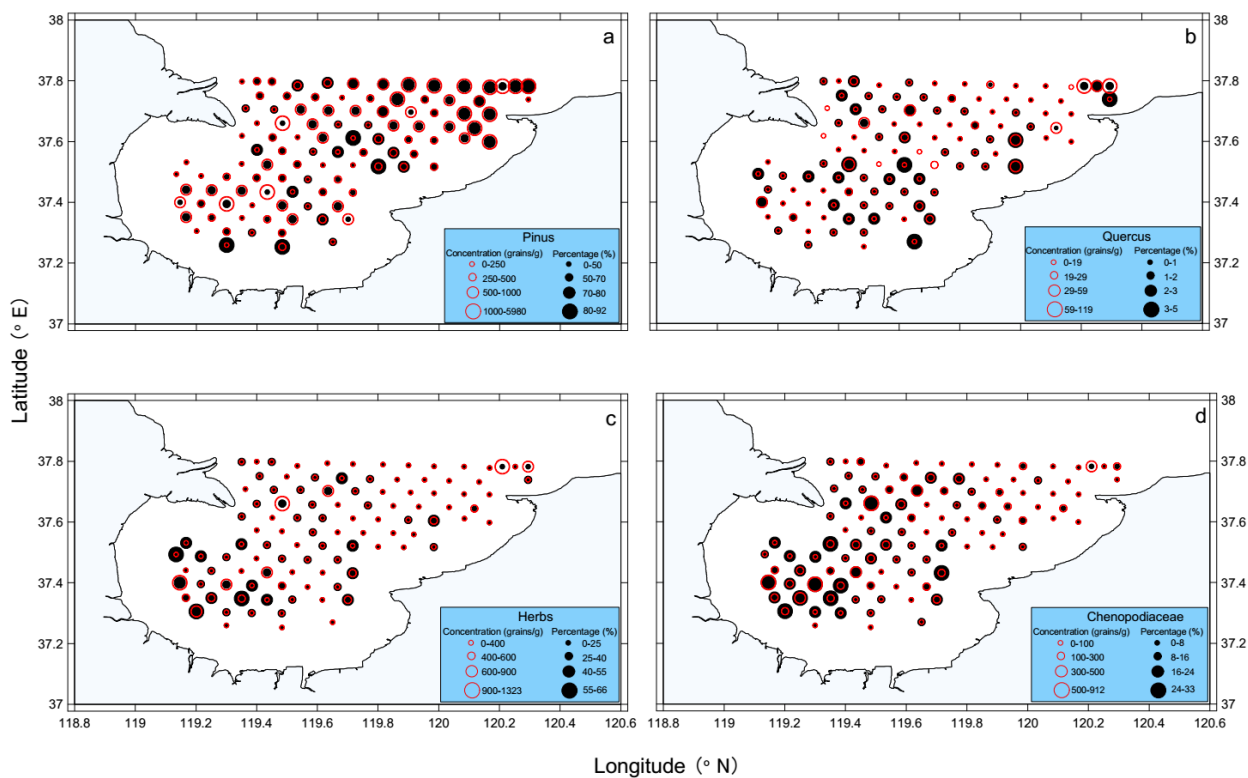




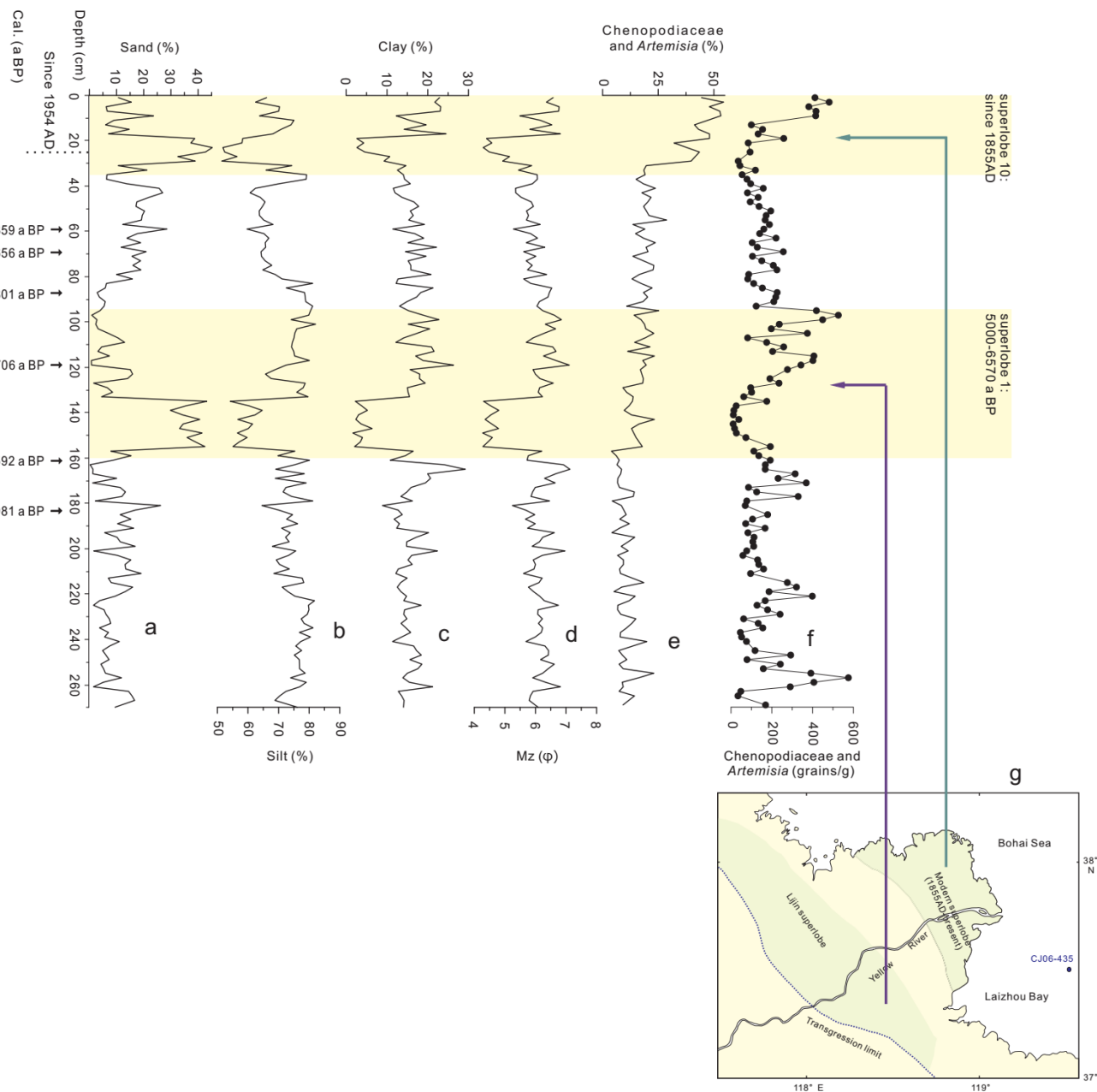
Figure 5



860  
861  
862  
863  
864  
865  
866  
867  
868  
869



Figure 6



870

871



Figure 7

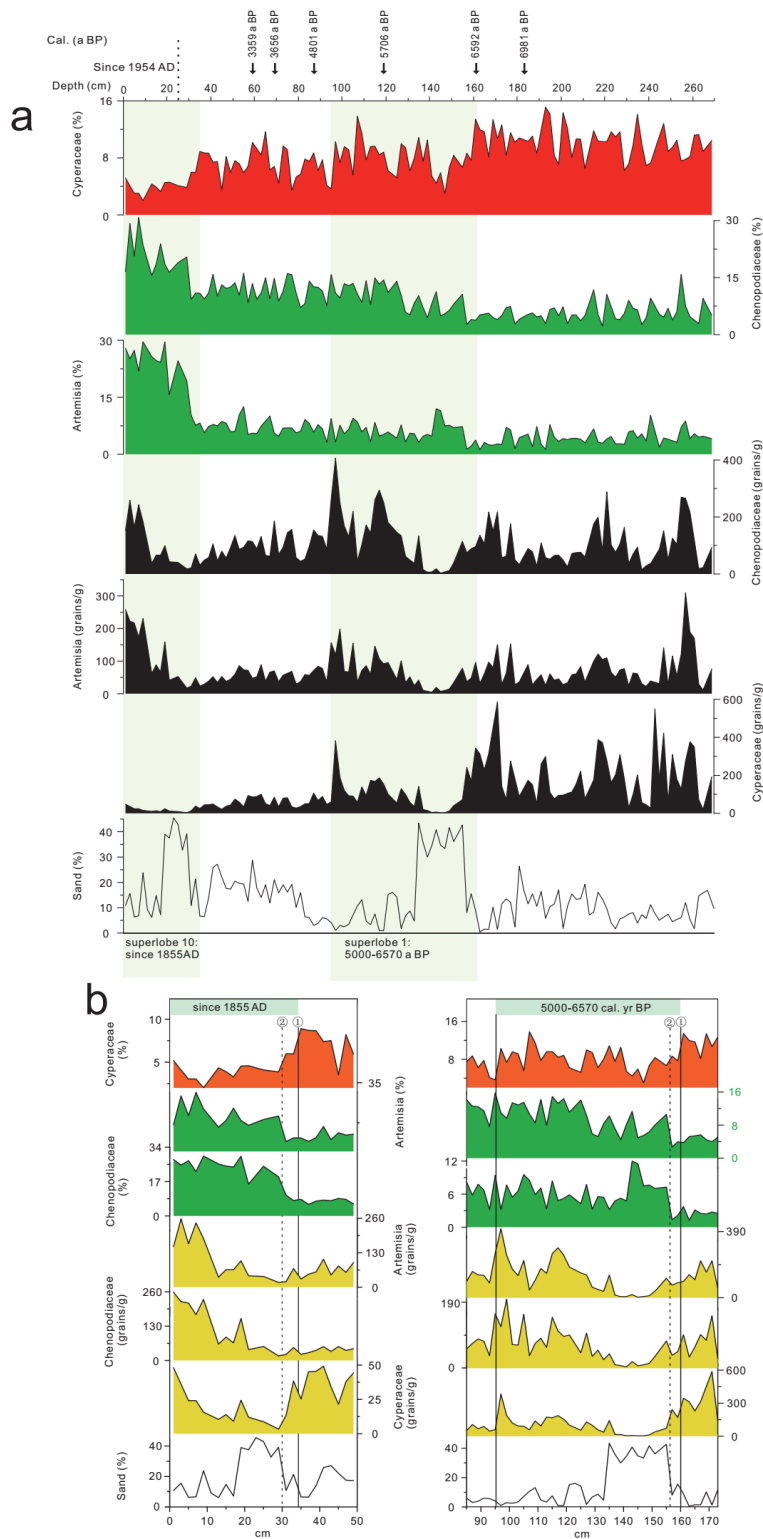




Figure 8

